Chapter 8

Investigations of nanophotonic waveguides and cavities for strong atom-photon interactions

8.1 Introduction

Following the pioneering work and field-opening advances in cavity quantum electrodynamics with single atoms and photons in Fabry-Perot optical cavities of more than two decades ago [236, 131, 132], leading to the demonstration of an elementary quantum network consisting of two nodes each composed of a single atom trapped in a Fabry-Perot cavity that exchange quantum information via entanglement [197], much research effort has been devoted to the issue of scalability and reliability for the realization of such a quantum network, which may consist of $N \gg 1$ nodes. Discussed previously in this thesis, and indeed a theme of this thesis, is the investigation of the realization of such a quantum network on an on-chip lithographically fabricated nanophotonic platform, which is a promising candidate for the realization of a scalable quantum network with $N \gg 1$ nodes. Unlike conventional Fabry-Perot cavities, here single atoms interact with single photons at distances in the scale of $\sim$ 100 nm from the surface of the on-chip photonic device. Advances in high quality lithographic nanophotonic devices [240, 73] have enabled the confinement of the electromagnetic field associated with a single photon into a small space, where one photon could interact strongly with a single atom located at $\sim$ 100 nm from dielectric photonic devices. The first realization of such strong single atom-photon interaction with an on-chip monolithic microresonator was demonstrated in 2006 [9], where a signature of strong atom-photon coupling was observed. In the work of this thesis described in Chapter 5, strong interaction between single atoms and photons was observed in 2011 via direct real-time measurements, revealing nonperturbative cavity QED effects such as vacuum

Rabi splitting, as well as perturbative atom-surface effects associated with the close proximity of the strongly coupled atoms to the dielectric microtoroidal photonic device [5]. Although the prospects of cavity QED with nanophotonic devices are promising, the challenges are great, as new issues previously absent in conventional Fabry-Perot cavities arise. For example, discussed in Chapter 5 are issues of atom-surface interactions that modify an atom's internal electronic structure, decay rates, and center of mass dynamics. The complex behavior of photonic mode field polarizations, and the achievement of both long atom-photon interaction time via atom trapping and strong atom-photon interactions, as discussed in Chapters 6 and 7, all are important challenges to overcome, in this transition towards a chip-integrated quantum network with nanophotonic devices.

As nanofabrication technology and techniques advance, in this chapter we discuss the use of lithographically fabricated nanophotonic waveguides and nanophotonic crystal cavities [115] as platforms for atom-photon interactions. The ability to lithographically fabricate increasingly advanced and higher quality devices [73, 39], monolithic and fully-integrated on a chip with fiber input-output coupling, offers potential for such a platform to move towards a scalable quantum network system. With direct fiber butt-coupling, small mode volume, potentially high cavity finesse, and control enabled by the photonic crystal band-structures, these systems offer potential for strong atom-photon interaction in a cavity QED setting; and moreover, also offer potential for other physics involving many-body interactions in one-dimension or two-dimensions, where exciting new ideas have been proposed for the investigation of self-organization dynamics of atomic lattices [40] and cavity QED using arrays of atoms as the mirrors [41]. In this chapter we start by discussing the device designs and expected atom-photon interaction strengths, cold atom clouds, cavity QED, our experimental setup (that compliments our discussion in Sec. 3.3), and atom trapping schemes.

The work discussed in this chapter is part of an on-going project that involves many individuals in multiple labs in our group and in the Painter group, whom I would like to acknowledge here. Firstly, in Lab 11: Akihisa Goban and Chen-Lung Hung who first implemented the multi-magneto-optical trap scheme to transport the atomic cloud from the source chamber, to the science chamber, and into the photonic device chip in our group, which was critical in forming the basis of our setup in Lab 1 (the lab that I worked in); our collaborator Kyung Soo Choi; and Jonathan Hood and Su-Peng Yu who closely worked with device characterization and fabrication with Sean Meneehan and Richard Norte in the Painter group. In Lab 2: Jae Hoon Lee, Juan Muniz, and Ding Ding. I would like to especially acknowledge Juan Muniz, with whom I have had the opportunity to closely collaborate, working on the atom trapping schemes discussed in this chapter. Last but not least, the team in our

lab, Lab 1, who directly work in the experimental setup discussed in this thesis; especially Andrew McClung, Pol Forn-Diaz, and Martin Pototschnig who have made great contributions and shared valuable insights critical to our experiment. I would also like to acknowledge Clement Lacroute from our group and Justin Cohen, Taofiq Paraiso, and Alex Krause in the Painter group. This work is carried out under the guidance and supervision of my advisor, Prof. Jeff Kimble, in collaboration with Prof. Oskar Painter at Caltech.

8.2 Platform

8.2.1 Nanobeam waveguides

This and later sections build upon our discussion in Sec. 3.3, where we consider two types of device. Firstly, we consider a single nanobeam with a photonic crystal [115] mirror at the end, and secondly a double nanobeam with a photonic crystal mirror at the end. We refer to the schematic of the single nanobeam in Fig. 3.11, and the double nanobeam in Fig. 3.13.

Consider the single nanobeam device illustrated in Fig. 3.11. The device design and mode field effective area are discussed in Sec. 3.3. Now recall that in Sec. 2.5.1, particularly Sec. 2.5.1.2, we discussed how the mode field effective area A_{eff} is related to atom-light interaction strength quantified by experimentally measurable quantities such as the transmittance and reflectance of a probing optical beam. Moreover, as discussed in Sec. 6.2.4, we know that the proximity of an atom to a dielectric surface leads to Casimir-Polder effects that modify the internal electronic states of the atom, leading to transition energy level shifts that vary with the atom's location. As an atom approaches a dielectric surface, the increasingly large level shift will eventually bring the atom's transition frequency to be detuned away from the probe light frequency (or cavity resonant frequency in a cavity QED system). In this section, we consider how these factors come together, and present our result for a single nanobeam waveguide of various sizes in Fig. 8.1.

We start from the mode field effective area A_{eff} for the fundamental x-polarized mode of a single nanobeam (Fig. 3.11) with height $h = 200$ nm, and width $w = 100$, 150, 200, 250, 300, 350, 400 nm as shown in Fig. 3.12. From this, using our model described in Sec. 2.5.1.2 and illustrated in Fig. 2.2, which takes into account complex electromagnetic field polarizations and modified decay (loss) rate, we compute Γ_{p} and Γ_0, the atomic decay rate into the guided photonic mode and decay (loss) rate to the environment (including the surface modes of the dielectric) respectively. Next, by applying the values of Γ_{p} and Γ_0 into equations (2.29) and (2.30), we calculate the transmittance

T and reflectance R of a probe (guided) light, set to be resonant to the free-space atom transition frequency $\omega_{\rm a}^0$, where the superscript 0 indicates that it is the free-space transition frequency.

Now as discussed earlier, as the atom gets closer to the dielectric surface, its transition frequency changes as a function of space, $\omega_{\rm a} = \omega_{\rm a}(\vec{r}_{\rm a})$, where $\vec{r}_{\rm a}$ is the atom's position. We include the effect of a Casimir-Polder induced transition frequency shift by modeling the $6S_{1/2}$ ground state level shift by a simple van der Waals potential $U_{\rm g} = C_3'/d^3$ where d is the atom-surface distance (along x or along y), with the coefficient $C_3' = \frac{n2^2-1}{n2^2+1}/\frac{n1^2-1}{n1^2+1}C_3$, where $C_3/h = 1178$ Hz.μm^3 is the coefficient for a cesium atom and a silicon dioxide (SiO_2) surface [228, 184], $n2 = 2.0$ is the refractive index of silicon nitride, $n1 = 1.45$ is the refractive index of silicon dioxide, and h is Planck's constant. We note that this model treats the dielectric surface as an infinite planar surface. For the $6P_{3/2}$ excited state, we approximate it as $U_{\rm e} = 2U_{\rm g}$ [142]. Since the excited state shift is greater in magnitude than the ground state shift, the atomic transition frequency decreases as the atom approaches the dielectric surface (as both the ground and excited states are red-shifted), $\omega_{\rm a} = (U_{\rm e} - U_{\rm g})/h$. The black curve in figure 8.1 (i) shows the ground state level shift $U_{\rm g} = C_3'/d^3$ for a cesium atom at a distance d from a silicon nitride surface. The red, green, and blue curves show scaled potential $A \times U_{\rm g} = A \times C_3'/d^3$ with $A = 1/2$, $1/3$, and $1/4$ respectively. For comparison, we show the connected black points, numerical result from a full Casimir-Polder calculation by Chen-Lung Hung using MIT MEEP software, which takes into account the finite geometry of the dielectric surface. In this calculation, a cesium atom is located at a distance d from the surface of a silicon nitride nanobeam structure with finite height $h = 200$ nm and essentially infinite length[1] [110]. As can be seen in Fig. 8.1 (i), the finite height of the nanobeam reduces the strength of the Casimir-Polder shift by around a factor of three, which is significant. As the atom moves closer to the surface of the nanobeam, the finite nanobeam surface will become increasingly large relative to the distance d, and thus the potential should approach that of $U_{\rm g} = A \times C_3'/d^3$ with $A \to 1$. Figures 8.1 (ii-iii) show the calculated level shifts $\omega_{\rm a} = A \times (U_{\rm e} - U_{\rm g})/h$ for the four cases $A = 1$, $1/2$, $1/3$, $1/4$ corresponding to the black, red, green, and blue curves respectively.

Finally, incorporating the above surface-induced atom transition frequency (using $A = 1/3$ in $\omega_{\rm a} = A \times (U_{\rm e} - U_{\rm g})/h$) into the transmittance T and reflectance R equations as described in the previous paragraphs above, we show in Fig. 8.1 b-e), the results for a cesium atom and a silicon nitride single nanobeam (Fig. 3.11) with height $h = 200$ nm and width $w = 100$, 150, 200, 250, 300, 350, 400 nm (colored in red, blue, green, magenta, brown, cyan, orange respectively), for an atom

[1] We note that the exact calculation is for a double nanobeam structure, with height $h = 200$ nm, separated by a gap 350 nm. As we are focusing on distances $d < 150$ nm where the level shifts are significant, we treat the contribution from the other surface, at distances > 200 nm, to be negligible.

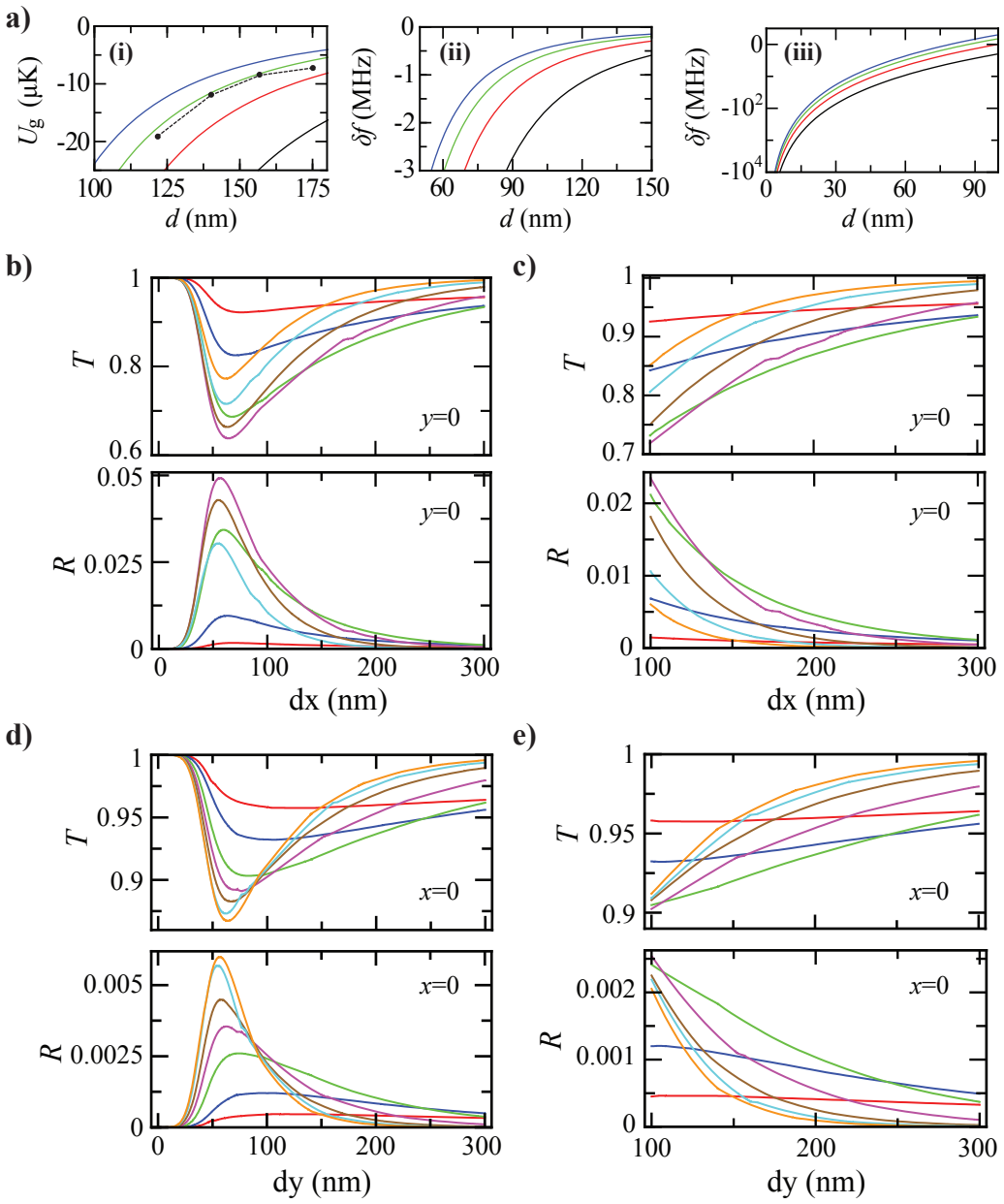

Figure 8.1: **Single nanobeam waveguide single atom transmittance and reflectance with atom-surface induced level shifts.** **a)** (i) Atom ground state Casimir-Polder level shift as a function of atom-to-surface distance d. Solid curves: $U_g = A \times C_3'/d^3$, where C_3' is the van der Waals coefficient for cesium and silicon nitride (infinite planar) surface, and $A = 1, 1/2, 1/3, 1/4$ for the black, red, green, blue curves respectively. The black data points are a full simulation taking into account the finite nanobeam's closest surface height (height $h = 200$ nm, infinite length), calculated using finite element method by Chen-Lung Hung [110]. (ii-iii) Atom's transition frequency shift δf due to differential level shift of the ground and excited state ($U_e = 2U_g$). **b-c)** Transmittance (T) and reflectance (R) of a single nanobeam waveguide with a single atom located at atom-to-surface distance along the x-axis (i.e., at $y = 0$), dx, for a single nanobeam with height $h = 200$ nm, and width $w = 100$, 150, 200, 250, 300, 350, 400 nm corresponding to the red, blue, green, magenta, brown, cyan, orange curves respectively. Part c) shows the same curves as part b) but across different range to highlight the longer distance behavior. **d-e)** Transmittance (T) and reflectance (R) of single nanobeam waveguide with a single atom located at atom-to-surface distance along the y-axis (i.e., at $x = 0$), dy, for a single nanobeam with height $h = 200$ nm, and width $w = 100$, 150, 200, 250, 300, 350, 400 nm corresponding to the red, blue, green, magenta, brown, cyan, orange curves respectively.

positioned along the x axis in b-c), and along the y axis in d-e). We note that the atom-photon interaction strength is higher for a double nanobeam structure, as can be seen from the larger λ^2/A_{eff} values for an atom located at the center of a double nanobeam structure (see Fig. 3.14) compared with an atom located at the evanescent field tails of a single nanobeam structure (see Fig 3.12).

8.2.2 Cold atoms

An important feature of the nanophotonic beam platform as illustrated in Fig. 8.2 a) (i) is the undercut through-hole of size ≈ 2 mm $\times$ 3 mm (see Fig. 3.11) that allows three-dimensional optical access and hence cooling and trapping of a thermal atom cloud within which the nanophotonic device is immersed. In contrast with other platforms such as an on-chip microtoroidal resonator (see Fig. 6.10), this reduces the complexity involved in creating a dense cold atom cloud, within the small volume of the nanophotonic evanescent field, as well as reducing the complexity involved in loading atoms into an optical trap while potentially allowing strong coupling between trapped single atoms and photons. As will be discussed in Sec. 8.2.4 and illustrated in Fig. 8.4, our scheme involves the creation of three magneto-optically trapped atom clouds going from the source chamber to the science chamber, and ending by going into the through-hole where the cloud overlaps with the nanophotonic beam. This final magneto-optical trap formed inside the through-hole of the chip, which we call a 'mini-MOT', is illustrated in Fig. 8.2 a) (i). In panel (ii) of the figure, a magnified view of one of the nanophotonic beam devices is shown together with the mini-MOT atom cloud. Next, in panel (iii), is a close-up of the center part of the nanophotonic device, where a uniform rectangular nanobeam of width w and height h is shown, together with the coordinate system $\{x, y, z\}$. Finally in (iv) we show the electric field amplitude $|E|$ profile for the fundamental x-polarized mode of a nanobeam with width $w = 300$ nm and height $h = 200$ nm. An atom within the thermal cloud will have a velocity v described by the Maxwell-Boltzmann distribution for a thermal gas of a certain temperature T_{cloud}, in addition, it experiences gravitational force F_{g}, optical cooling (Doppler cooling, polarization-gradient cooling) and trapping forces from the mini-MOT beams along the three-dimensions F_{opt}; and close to the surface of the nanobeam it experiences Casimir-Polder surface attractive force F_{s}. Also shown in Fig. 8.2 a) (iv), is the approximate rectangular cross-sectional area of the evanescent field mode at one side of the nanobeam, of size x0 $\times$ y0.

Figure 8.2 b) shows a plot of number of atoms N_{atoms}, as a function of atom cloud density ρ, that lie within a volume of $V = V_0 = 2\times$ x0 $\times$ y0 $\times$ L, where x0 = 100 nm, y0 = 100 nm, and L = 500 μm. The factor of two takes into account the two sides of the nanobeam, and L represents

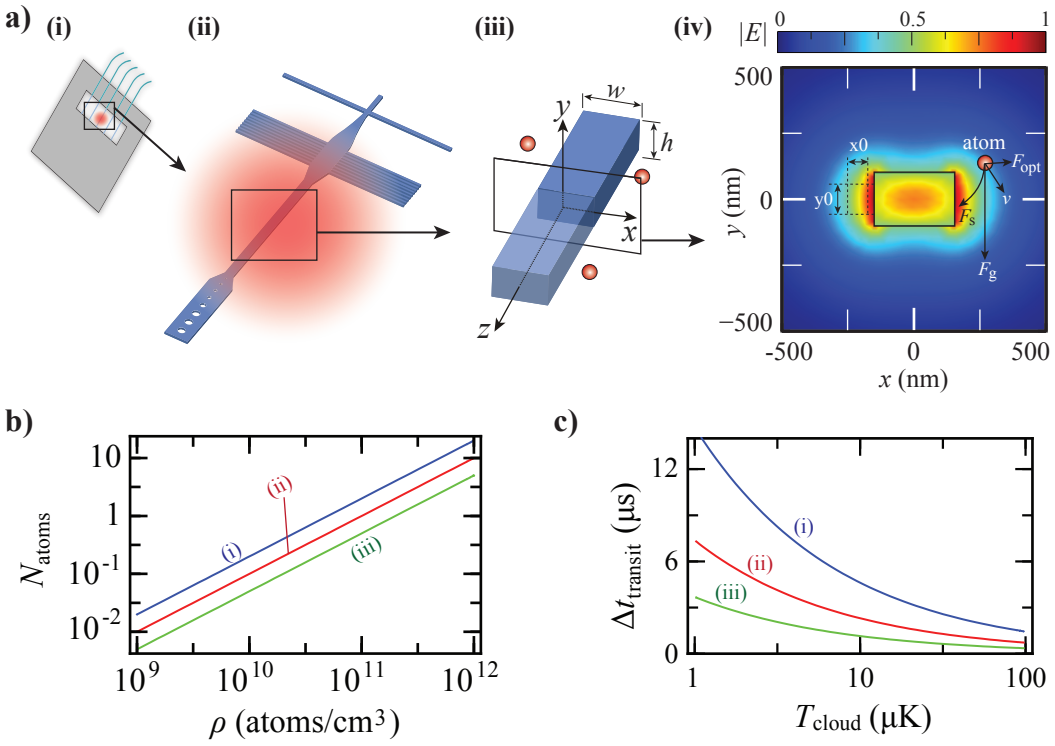

Figure 8.2: **Cold atom cloud near a single nanobeam structure. a)** Schematic of a silicon chip with a 3 mm × 1.5 mm through-hole with five nanophotonic devices butt-coupled to five optical fibers, and a cold atom cloud overlaping the center device, shown in (i). Part (ii) shows a close look of the center single nanobeam photonic device with butt-coupler at one end, a photonic crystal mirror at the other end, and a cold atom cloud centered on the uniform nanobeam waveguide section at the center. Part (iii) shows a schematic of the single nanobeam waveguide, showing the nanobeam's width w, height h, and the coordinate system $\{x, y, z\}$. Part (iv) shows the fundamental x-polarized mode normalized electric field amplitude $|E|$ for a single nanobeam of width $w = 300$ nm and height $h = 200$ nm. The mode area in this $x - y$ cross-sectional plane is approximated by the rectangle of width x0 and height y0 as illustrated. An atom nearby this silicon nitride nanobeam has an initial velocity v associated with the thermal cloud velocity distribution for a given temperature T_{cloud}, several forces acting on the atom including gravity (F_{g}), surface force (F_{s}), and optical forces (F_{opt}) from the magneto-optical trapping and cooling beams. **b)** Number of atoms (N_{atoms}) that are on average in the vicinity of a single nanobeam's evanescent field region as a function of atom cloud density (ρ), located within a volume of $V = V_0 = 2\times$ x0 × y0 × L, where x0 = 100 nm, y0 = 100 nm, and $L = 500$ μm for the red curve (labeled (ii)). The curves labeled (i) and (iii) in blue and green correspond to twice ($V = 2V_0$) and half ($V = 0.5V_0$) volumes respectively. **c)** Transit time ($\Delta t_{\mathrm{transit}}$) of an atom with an initial rms velocity v directed downwards, which is accelerating in gravity, not taking into account surface (F_{s}) nor optical (F_{opt}) forces. The curves labeled (i), (ii), (iii) in blue, red, green correspond to an atom falling down over a distance y0 = 200, 100, 50 nm respectively, where $\Delta t_{\mathrm{transit}}$ is the time the atom takes over the distance y0.

the length of the nanobeam (we note that in this simple model we do not include the parts of the evanescent field at the top and bottom of the nanobeam, along the y axis). This rough estimate is shown by the red curve labeled (ii) in Fig. 8.2 b), giving a sense of the atom cloud density required. The curves labeled (i) and (iii) in blue and green correspond to twice ($V = 2V_0$) and half ($V = 0.5V_0$) volumes, respectively. Here, the number of atoms N_{atoms} represents the average steady-state number of atoms present within the volume V at any point in time. In Fig. 8.2 c), we show the transit time of an atom (with an initial rms velocity v set by the cloud temperature T_{cloud} according to Maxwell-Boltzmann distribution and assumed to be directed downwards) which is accelerating downwards due to gravity at the rate $g = 9.81$ m/s^2. In this simple model, we do not take into account the optical cooling and trapping forces F_{opt} nor the surface forces F_{s}. The curves labeled (i), (ii), (iii) in blue, red, and green correspond to an atom falling downwards over a distance y0 = 200, 100, 50 nm respectively. The transit time $\Delta t_{\mathrm{transit}}$ is the time that the atom takes to accelerate through the corresponding distance y0. More precise calculation of transit times can be performed by simulation of ensemble of atoms with randomly distributed velocities, positions, optical forces, scattering rates, magnetic fields, polarization gradient cooling efficiencies, calculations of Casimir-Polder attractive potential for the nanobeam geometry, etc. While some aspects would increase the transit time, such as optical cooling forces and the fact that the atom velocities are uniformly distributed over 2π steradians instead of the extreme case of purely downward velocity considered here, other aspects would reduce the transit time, such as attractive surface forces that pull the atoms into the nanobeam surfaces.

As discussed above and in Fig. 8.2, we see that it is crucial to have as high an atom cloud density as possible, especially for a nanobeam waveguide device without a cavity where the atom-photon coupling strength may not be very high: since in this case we do not have sufficient signal associated with the transit of a single atom, and the measurements rely on ensemble averaging. In this regime, we now discuss the optimization of probe beam pulse length $\Delta t_{\mathrm{probe}}$. In the regime where $N_{\mathrm{atoms}} \geq 1$, i.e., $\rho \geq 10^{11}$ atoms/cm^3, at any given time one finds on average at least one atom coupled to the waveguide. Here, the probe pulse length is not as sensitive in determining the signal-to-noise ratio of the measurement. In the more experimentally typical regime $\rho < 10^{11}$ atoms/cm^3 however, $N_{\mathrm{atoms}} < 1$, and one needs to integrate in time in order to have at least one atom coupled to the probe beam. Given the transit time scales of $\Delta t_{\mathrm{transit}} = 1$-$10$ μs, in principle the largest signal to noise can be achieved by having the probe beam pulse time $\Delta t_{\mathrm{probe}} \leq \Delta t_{\mathrm{transit}} = 1 - 10\mu$s, such that an atom is coupled during the entire pulse time of $\Delta t_{\mathrm{probe}}$. This however requires knowing the

time at which the atom gets coupled to the photonic mode, something which may not be possible with limited atom-photon coupling strength. With these factors, one optimizes the probe pulse time $\Delta t_{\rm probe} > \Delta t_{\rm transit}$, which should be larger than the transit time, to increase the probability that an atom is coupled to the photonic mode during the duration of the probe pulse, but not so large such that increasing the pulse time leads to a larger fraction of the pulse time where there is no atom coupled. Highest signal-to-noise ratio of the overall ensemble averaged measurement (say of transmittance T or reflectance R) can be reached following the optimization. The case is different in a regime where atom-photon coupling strength is sufficiently large such that a single atom transit leads to a measurable signal, such as the case in the microtoroid cavity QED system. Here, one could time-reference measurement ensemble averages to the transit start time $t_{\rm transit}$ when the atom first becomes coupled to the photonic mode. As discussed in Sec. 6.3.2.1, this real-time trigger could also be used to load atoms into a conservative optical trap.

8.2.3 Cavity QED with nanobeams

In this section we focus on a cavity QED system with a single nanobeam waveguide with a pair of photonic crystal mirrors at its ends, similar to the design illustrated in Fig. 3.11 with one additional photonic crystal mirror. Our calculations in this section are based on the equations and approach discussed in Sec. 2.4.1 and Sec. 2.4.2, with the electric field mode profile of a rectangular single nanobeam waveguide as described in Fig. 3.11. We consider a single silicon nitride (refractive index $n = 2.0$) nanobeam waveguide with width w and height $h = 200$ nm, with a pair of photonic crystal mirrors at each end, forming a linear optical cavity of length $L_{\rm cav} = 500$ μm. We consider a modest cavity finesse of $\mathscr{F} = 100$ which is within current fabrication capability, at cesium D2 line, $\lambda =$ 852 nm, for the x-polarized mode. This leads to a free-spectral-range of FSR $= c/(2nL_{\rm cav}) = 148.8$ GHz (or 0.36 nm), where we use an effective[2] refractive index of $n = 2.0$, and c is the speed of light. With the finesse $\mathscr{F} = 100$, giving a cavity quality factor of $Q = \mathscr{F}\nu_{\rm a}/{\rm FSR} = 2.37 \times 10^5$, (where $\nu_{\rm a} = 352$ THz is the atom's transition frequency) the cavity total decay rate $\kappa = \pi c/(\lambda Q)$ $= 4.67$ GHz. Now from COMSOL finite element calculation, we compute the electric field profile of the single nanobeam (e.g., shown in Fig. 3.11), which combined with the optical cavity parameters above, allow the computation of the cavity QED parameters including the mode volume $V_{\rm m}$, atom-

[2]Strictly speaking, a more precise number for n is the group refractive index, $n_{\rm g}$, calculated for the guided mode, which takes into account the dispersion. The group refractive index is given in terms of the phase effective index, $n_{\rm eff}$, by $n_{\rm g} = \left(\omega \frac{dn_{\rm eff}}{d\omega} + n_{\rm eff}\right)$, where $n_{\rm eff}$ is the phase effective index (calculated for example by COMSOL). See the footnote in Sec. 2.5.2.3 for this derivation. The group index depends on the exact dimensions of the waveguide. For example, for a single SiN nanobeam with height $h = 200$ nm and width $w = 300$ nm, $n_{\rm g} = 2.06$ at $\lambda_0 = 852$ nm, the free-space wavelength. Here, $\frac{dn_{\rm eff}}{d\omega} = 3.90 \times 10^{-4}$ THz^{-1} and the phase effective index is $n_{\rm eff} = 1.19$.

photon coupling strength $g = g(\vec{r_a})$, cooperativity parameter $C = C(\vec{r_a})$, and critical atom N_{ca} and photon N_{cp} numbers. The equations for all of these parameters are explicitly given and discussed in Sec. 2.4.2. We note that in the calculations in this section, as was the case in the calculations in Sec. 2.4.2, we use the transverse atomic dipole decay rate $\gamma_{0\perp}/2\pi = 2.61$ MHz.

Figures 8.3 a-b) shows the cooperativity parameter C as a function of the atom-to-surface distance along the x-axis ($y = 0$), dx, for a single nanobeam with the above parameters, with nanobeam height $h = 200$ nm, and width $w = 100$, 150, 200, 300, 400 nm for the green, magenta, black, red, blue curves respectively. We see that the largest cooperativity parameter C near the surface (i.e., for small dx) is given by a nanobeam with $w \times h = 300$ nm $\times$ 200 nm. Our initial fabricated single nanobeam devices have these cross-sectional dimensions. In the following parts of the figures, i.e., Fig. 8.3 e-h), we use these nanobeam dimensions: $w \times h = 300$ nm $\times$ 200 nm. Figures 8.3 e-f) show cross-sectional plots along x-axis, as a function of the atom-to-surface distance, dx, and figures 8.3 g) and h) show cross-sectional plots along y direction at dx = 0 and at dx = 100 nm, respectively. Figures 8.3 e-h) show the atom-photon coupling parameter g and the critical atom and photon numbers, N_{ca} and N_{cp}. Here, the blue (and cyan) curves correspond to a cavity length $L_{cav} = 500$ μm and finesse $\mathscr{F}$ = 1000, the red (and magenta) curves correspond to a cavity length of $L_{cav} = 250$ μm and finesse $\mathscr{F}$ = 1000, and the black curves correspond to a cavity length $L_{cav} = 250$ μm and finesse $\mathscr{F} = 2000$. The horizontal lines show the corresponding (color-coded) total cavity decay rates κ.

We note that the approach in this section is applicable to a double nanobeam structure with photonic crystal mirrors, which offers higher atom-photon coupling strength due to the electric field mode profile as discussed in Sec. 8.2.1. An even higher atom-photon coupling strength could potentially be achieved by positioning single atoms directly inside the holes of a photonic crystal cavity, where small mode volume and low mode group velocity associated with the band-structure provide enhancement to the atom-photon interaction strength [110].

8.2.3.1 Cavity temperature tuning

We consider the effect of temperature change to the effective optical path length in our silicon nitride (dielectric) nanophotonic cavity. In general for any dielectric material, there are two first-order components that change in response to temperature changes, namely the refractive index (n) of the dielectric material, and the physical length (or size) of the material (L). More quantitatively,

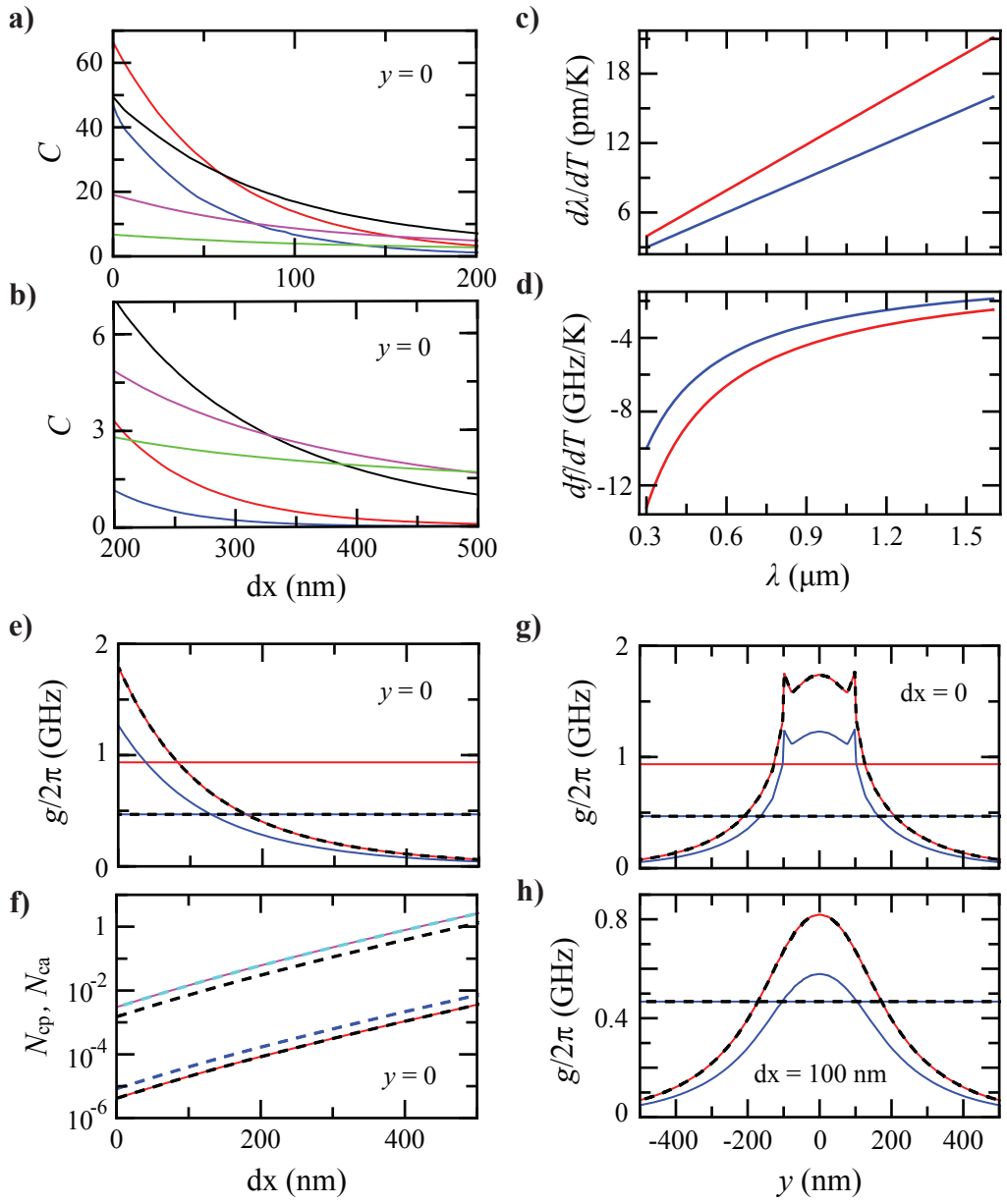

Figure 8.3: **Cavity QED with a single nanobeam and cavity frequency temperature tuning. a-b)** Cooperativity parameter C as a function of the atom-to-surface distance along the x-axis ($y = 0$), dx, for a cesium atom (D2 transition, $\lambda = 852$ nm), for a single nanobeam x-polarized mode, with cavity length $L_{\rm cav} = 500$ μm and finesse $\mathscr{F} = 100$ (giving cavity FSR = 149 GHz (or 0.36 nm), quality factor $Q = 2 \times 10^5$, and cavity decay rate $\kappa/2\pi = 4.67$ GHz), with nanobeam height $h = 200$ nm, and width $w = 100$, 150, 200, 300, 400 nm for the green, magenta, black, red, blue curves respectively. **c-d)** Tuning curves of wavelength and cavity resonance frequency as a function of wavelength λ, based on thermo-optic ($\frac{dn}{dT}$), thermal expansion ($\frac{dL}{dT}$) coefficients for silicon nitride, $\frac{dn}{dT} = 10^{-5}$ K^{-1}, $\frac{dL}{dT} = 0$ and 3.2×10^{-6} K^{-1} for the blue and red curves respectively. **e)** Atom-photon coupling rate g. **f)** Critical atom and photon numbers, $N_{\rm ca}$ and $N_{\rm cp}$. **g-h)** Atom-photon coupling rate g as a function of the y coordinate, at dx = 0 in g) and at dx = 100 nm in h). In parts e-h), the blue (and cyan) curves correspond to a cavity length $L_{\rm cav} = 500$ μm and finesse $\mathscr{F} = 1000$, the red (and magenta) curves $L_{\rm cav} = 250$ μm and finesse $\mathscr{F} = 1000$, and the black curves $L_{\rm cav} = 250$ μm and finesse $\mathscr{F} = 2000$. The horizontal lines show the corresponding (color-coded) total cavity decay rates κ. Note that the single nanobeam is symmetrically centered at the origin ($x = y = 0$) in the $x - y$ cross-section, with its axis going out-of-page along the z-axis, as illustrated in Fig. 3.11. Note: Here we do not include Casimir-Polder effects.

the change in effective wavelength (λ) of a propagating light inside the dielectric is given by [134]:

$$\frac{d\lambda}{dT}(\lambda, \frac{dn}{dT}, \frac{dL}{dT}) \approx \lambda \frac{dn}{dT} + \lambda \frac{dL}{dT}, \tag{8.1}$$

where $\frac{dn}{dT}$ is the thermo-optic coefficient, $\frac{dL}{dT}$ is the thermal expansion coefficient, λ is the effective optical wavelength in the cavity or waveguide, and in terms of optical frequency (f), $\frac{df}{dT} = -\frac{c}{\lambda^2}\frac{d\lambda}{dT}$. Note that the values of the thermal coefficients could depend on the exact mechanical properties of the system, such as its geometry and any mechanical stresses. Table 8.1 lists the thermal coefficients for silicon dioxide (SiO_2) and silicon nitride (SiN). The values for SiO_2 are from [134]. For SiN, we find a range of theoretical values quoted for the thermo-optic coefficient ($\frac{dn}{dT}$), as can be found from [160, 253, 104]. These values are listed in the first two columns of values in Table 8.1. In the third column, we include a specific case with $\frac{dn}{dT} = 10^{-5}$ K^{-1} and $\frac{dL}{dT} = 0$, which gives the limit of no thermal expansion, for example, in certain systems with strong mechanical compressions or geometrical constraints that inhibit mechanical expansion. For example, in certain experimental systems, the overall thermal coefficients $\frac{d\lambda}{dT}$ have been measured to have relatively low values, namely $\frac{d\lambda}{dT} = 12$ pm/K @1550nm (i.e., 6.6 pm/K @852nm) for a silicon nitride microdisk [19], and $\frac{d\lambda}{dT} = 16.6$ pm/K @1310nm (i.e., 10.7 pm/K @852nm) for a slot-waveguide silicon nitride ring resonator immersed in liquid and in contact with SiO_2 substrate [97].

Table 8.1: Thermo-optic (dn/dT) and thermal expansion (dL/dT) coefficients for silicon dioxide (SiO_2) and silicon nitride (SiN). As the effective wavelength λ increases as temperature increases, the effective optical frequency f decreases.

	SiO_2	SiN	SiN with $dL/dT = 0$
dn/dT	1.28×10^{-5} K^{-1}	$10^{-5} - 4.10^{-5}$ K^{-1}	10^{-5} K^{-1}
dL/dT	5.5×10^{-7} K^{-1}	3.2×10^{-6} K^{-1}	0
$d\lambda/dT$ @ 852nm	10 pm/K	$11 - 37$ pm/K	8.5 pm/K
$\lvert df/dT \rvert$ @ 852nm	4.7 GHz/K	$4.6 - 15.2$ GHz/K	3.5 GHz/K

Figures 8.3 c-d) show the coefficients $\frac{d\lambda}{dT}$ and $\frac{df}{dT}$ as a function of optical wavelength λ, for SiN, using the values $\frac{dn}{dT} = 10^{-5}$ K^{-1}, $\frac{dL}{dT} = 0$ and 3.2×10^{-6} K^{-1} for the curves colored in blue and red, respectively. For our silicon nitride cavity discussed at the beginning of Sec. 8.2.3, with cavity length $L_{\text{cav}} = 500$ μm, the free-spectral-range is FSR $= \frac{c}{2nL_{\text{cav}}} = 148.8$ GHz (or 0.36 nm), where we have used $n = 2.0$. Using $\frac{d\lambda}{dT} = 8$ pm/K @852nm, a temperature tuning range of ≈ 45 Kelvins is required to tune over one cavity FSR. In the case of our silica microtoroid system, we tuned the chip temperature up to 373 Kelvins (100° C) using a Peltier, and for higher bandwidth we used a small dynamic range laser heater focused onto the silicon chip substrate. Here, in this

case of nanophotonic beam cavity, temperature tuning may be more challenging as heat conduction through direct material contact is very small (e.g., the rectangular cross-section of the nanobeam is only 300 nm $\times$ 200 nm, while the overall structure length is in the order of $\sim$ millimeters). Similarly to the microtoroid case, the system is located inside a vacuum environment that limits heat convection by air molecules. Heat transfer may need to rely on radiative mechanisms, which would also be quite small. It may be possible to tune the temperature relatively slowly, such that a steady-state condition where the heat gain rate is equal to the heat loss rate is achieved. This may require higher resolution heat source and temperature sensing feedback. In addition to Peltier element and external laser heating, heating by injecting light into the guided mode could serve as a heat source. In our microtoroid experiment, we use a thermistor to give rough (large dynamic range) temperature feedback, which allows the Peltier to be servoed, and we use real-time cavity optical spectrum monitoring to obtain temperature feedback with a higher bandwidth. Together with this feedback time and our locking loop, our laser heating for the microtoroid experiment can reach about 8 Hz bandwidth, which is sufficiently fast relative to the relevant drifts of the cavity. During operation, we are able to maintain a cavity transmission darkness of $< 1\%$, limited by the mechanical vibrations between the microtoroid chip and the tapered nanofiber.

8.2.4 Experimental setup

Our experimental setup is shown in Fig. 8.4 a-d), which as discussed in Sec. 3.3.3, consists of two chambers, the source chamber (labeled a), and the science chamber (labeled e), separated by a distance of about L1 = 70 cm. This separation ensures a lower cesium background pressure in the science chamber and importantly, this keeps the nanophotonic device chip separated from the cesium source getter. This separation is critical in maintaining the quality of the nanophotonic device chip. For example, in our microtoroid experiments with a single chamber system [9, 57], the quality factors of the microtoroid cavities could degrade significantly in a few months, but with a two chamber system as discussed in Sec. 3.1.2 [5, 10], we could maintain the quality factors for more than 6-12 months. The combination of 5/8 inch inner diameter fittings and large standard 2.75 inch fittings (labeled b, c, d in Fig. 8.4 a,b)) over a total length of 18.5 inches gives a differential pressure ratio of ≈ 10. Our cesium getter[3] in the source chamber (labeled a) gives a background pressure of $\sim 10^{-9}$ torr, so that with the differential pressure ratio of 10, we have a background pressure of $\sim 10^{-10}$ torr in the science chamber (labeled e). Our typical MOT loading time is

[3]Note that one practical advantage of Cesium getter source is the lower background pressure ($\approx 10^{-9}$ torr) compared to an ampoule source ($\approx 10^{-7} - 10^{-8}$ torr).

around 3 to 5 seconds, consistent with a background pressure of $\sim 10^{-9}$ torr [13]. We note that higher differential pressure ratios are achievable by using a differential pumping tube that has a much smaller diameter (e.g., $\approx$ mm) than our tubes. However, this configuration may be sufficient especially for the purpose of maintaining the quality of the nanophotonic device chip, and with the sample and all the mounting support inside the science chamber, going to a background pressure of $\sim 10^{-11} - 10^{-12}$ torr may be difficult. One advantage of this large inner diameter tube is in the alignment of the pushing beam that transports atoms from the source chamber to the science chamber. As shown in Fig. 8.4 b), our ion pump (labeled f in figure) for the science chamber (labeled e) is positioned at quite a large distance from the chamber (L2 $\approx$ 70 cm), to suppress stray magnetic fields from the ion pump (Agilent-Varian VacIon Plus 40) which could reach 27 Gauss just outside of the ion pump box, decays to about 19 Gauss halfway between the ion pump and science chamber, and then decays to about 0.6 Gauss at the side of the science chamber (labeled e) closest to the ion pump, and 0.3 Gauss at the side of the chamber furthest from the ion pump.

We now discuss the steps involved in our experimental sequence starting from the source magneto-optical trap (MOT) to the mini magneto-optical trap (mini-MOT) cloud inside the through-hole of the nanophotonic device chip. In operation, our source magneto-optical trap quadrupole magnetic field and MOT beams ($\approx$ 10 MHz red-detuned from cesium (F=4 $\rightarrow$ F'=5) D2 line) including repumper beam at (F=3 $\rightarrow$ F'=4) transition are constantly turned on, generating $\sim 10^7 - 10^8$ atoms with density $\sim 10^9$ atoms/cm^3. Our source chamber quadrupole magnetic coil pair has 120 turns (each coil) with a radius of 45 mm and distance between the two coils being 200 mm. With a current of 18 A, it produces a magnetic gradient at the center along the coil axis of 10.4 Gauss/cm (for reference, each coil's resistance is 0.6 ohms). With this MOT cloud in the source chamber present, a push-beam (beam diameter $\approx$ 1 mm, slightly diverging, blue-detuned from (F=4 $\rightarrow$ F'=5) D2 line by +10 MHz, with a power of 3 mW) pierces through the MOT cloud, transporting atoms towards the science chamber. The push-beam is pulsed at 1 kHz, with a duty cycle of 30% on and 70% off. These numbers resulted from empirical optimizations. The purpose here is to give approximate parameter values. The push-beam pulse is activated for a period of 1 second, and during this time, the MOT beams in the science chamber are turned on (three retroreflected beams of diameter $\approx$ 2 cm, each with an optical power of 20 mW, -12 MHz detuned from (F=4 $\rightarrow$ F'=5) D2 line) and the quadrupole field (current 10 A, quadrupole coil diameter 7.5 inches, distance between two coils is 5.5 inches, and each coil has about 110 turns). This loads about 10^7 atoms into the MOT in the science chamber, with a density of $\approx 2 \times 10^{10}$ atoms/cm^3 (maximum absorption optical depth =

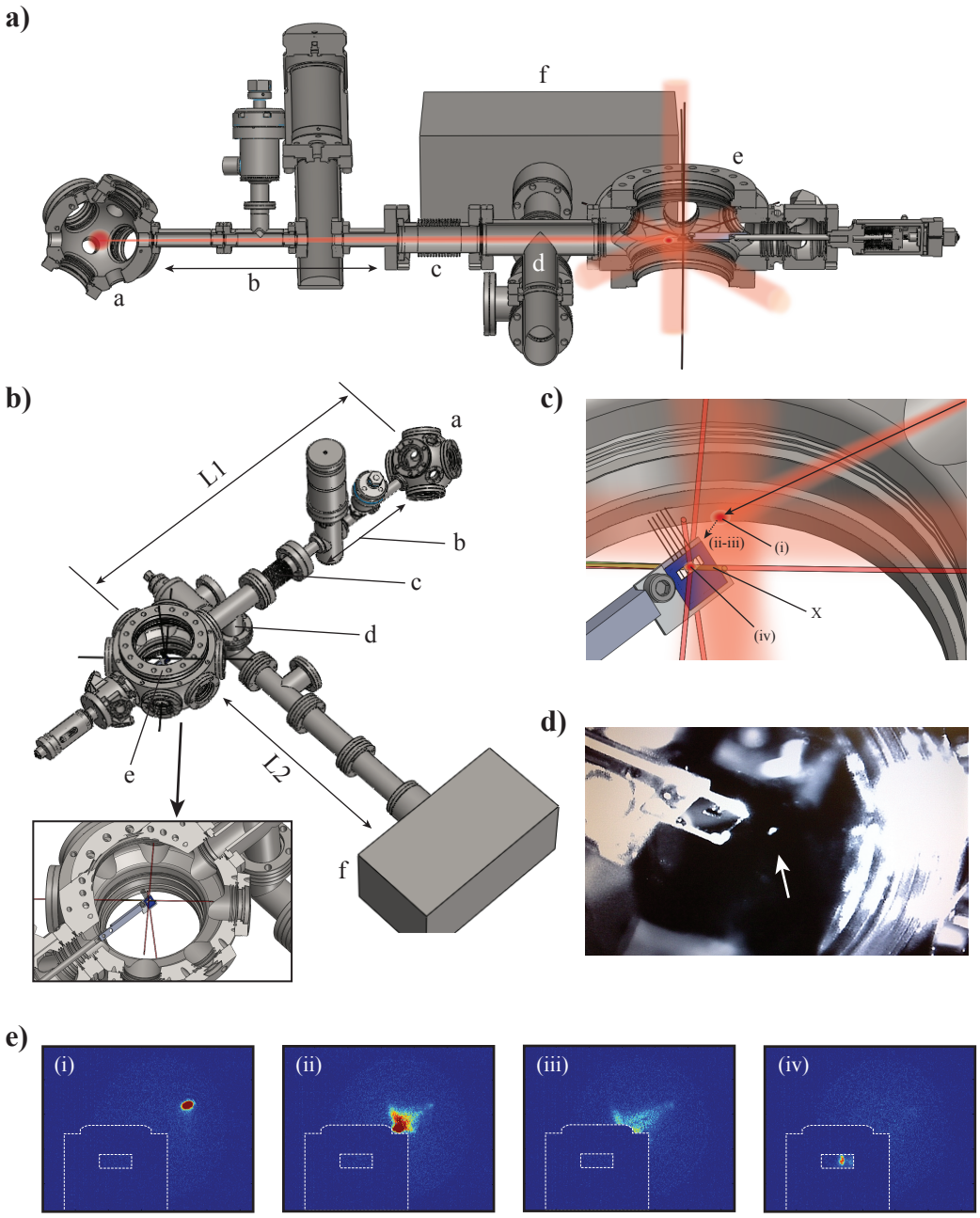

Figure 8.4: **Experimental setup. a-b)** A magneto-optically trapped (MOT) cloud of atoms is formed in the source chamber (a), pushed by near-resonant beam towards the science chamber (e) through a weak differential pumping tube (b), bellow and fittings (c-d), over a distance L1 $\approx$ 70 cm. The source and science chambers have background pressures of $\sim 10^{-9}$ torr and $\sim 10^{-10}$ torr respectively. Chamber (e) is continuously kept at ultra-high vacuum by the ion pump (f), located at L2 $\approx$ 70 cm. Atoms transported from the source chamber are collected at the science chamber by a second MOT with three orthogonal large ($\approx$ 2 cm diameter) retroreflected beams. **c)** After a compression stage, the atom cloud (i) is transported (ii-iii) into the through-hole of the chip where the device is (iv) by moving the quadrupole magnetic field zero from (i) to (iv). The atoms are then collected by a third MOT, a mini-MOT, formed by three orthogonal small ($\approx$ 1 mm diameter) retroreflected beams intersecting at the center of the chip's through-hole. Here, about $\sim 10^6$ atoms are collected (density $\sim 10^{10}$ atoms/cm^3). **d)** Fluorescence image showing the second MOT in chamber (e). **e)** Absorption images showing atom cloud transport starting from the second MOT location (i), during transport (ii-iii), and the mini-MOT location inside the chip's through-hole (iv).

5.7 at center of Gaussian cloud). Note that an important factor in the optimization, which depends on push-beam parameters, science chamber quadrupole field and MOT beams' parameters, is the atoms' velocities at the science chamber, which need to be within the capture velocity of the science MOT [171, 226]. Following this MOT cloud creation in the science chamber, we compress the atom cloud by changing the MOT and repumper beam parameters in the science chamber [58]. This process is performed over 40 ms, where in this process, the MOT beams are detuned from -12.5 MHz to -54.5 MHz, the MOT beams' power are attenuated from 20 mW (each beam) to 2.7 mW (recall that the MOT beam diameter is about 2 cm). Also during this 40 ms, the repumper beams' power is attenuated from 2 mW to about 0.27 mW, and the detuning is kept constant. After this compression stage, the atom density increases to $\approx 4 \times 10^{10}$ atoms/cm^3 but the number of atoms goes down from 10^7 atoms to $\approx 4 \times 10^6$ atoms.

Following the compression stage, we transport the atom cloud from the MOT position in the science chamber (after compression), into the through-hole of the nanophotonic device chip. This is done by changing the location of the quadrupole magnetic field zero by adjusting the electronic currents going through the three Hemlholtz bias coils (in x, y, z directions). The two (x and y) pairs of horizontal bias coils have an approximately rectangular cross-section coil shape with width 3.5 inches and height 2.25 inches, each of the four coils having 70 turns. The rectangular shape is not ideal but is chosen for practical reasons. The distance between the two coils for each pair is 11.50 inches, and the two pairs of coils are positioned such that their axes are orthogonal to each other. The vertical bias coil has a circular cross-sectional shape, with a diameter of 5 inches, each coil has 40 turns, and the distance between the two coils is 5 inches; it is quite close to the ideal Helmholtz configuration. To bring the zero of the quadrupole field from the initial science chamber MOT center location to the center of the through-hole of the photonic device chip, we change the current in x, y, z by $\{I_x, I_y, I_z\} = \{-3.47, -4.74, -0.9\}$ amps. Using the above parameters for the coils, these numbers can be converted into magnetic field amplitudes. Note that the distance between the inital science MOT position and the final mini-MOT (inside the chip) position is about 10-15 mm. We find that this transport of MOT cloud by changing of quadrupole magnetic field zero technique has quantized directions where the transport occurs efficiently. In our system, our Helmholtz bias magnetic coil axes (i.e., along the x, y, z-axes) are parallel to the corresponding MOT/repumper beam axes (along the x, y, z-axes). We find that the transport occur efficiently in the eight directions of the $x = y = z$, $x = y = -z$, $x = -y = z$, and $x = -y = -z$ axes (two directions for each, giving a total of eight directions). The brief reasoning for this is although the transport is facilitated by

the imbalance of the MOT beams following the move of the quadrupole zero location, leading to a net radiation pressure force towards the transport direction, this transport simultaneously requires efficient cooling such that the atoms do not heat up and escape during the transport. This cooling process is velocity-selective, and it is most efficient only in the eight aforementioned directions, hence the overall quantized transport directions. The details of this mechanism can be found in [218, 242, 221].

Now to get back to our time sequence. Immediately after the end of the 40 ms compression period, we ramp our MOT beam detuning to be closer to resonance over 5 ms and increase the power of the MOT and repumper beam by about 0.4 mW and 40 μW respectively. At the end of the 5 ms, we then execute the switch of the electronic currents of the three Helmholtz bias-coils, moving the quadrupole magnetic field zero. The atom cloud is then pushed towards the new quadrupole zero location (by the MOT beams that are still on at this stage). After 3 ms, we turn off the MOT and repumper beams. At this stage, the atom cloud is moving balistically towards the chip (new quadrupole zero location). It takes 10 ms for the cloud to arrive at the chip through-hole, about 10-15 mm away from the initial location. We note that strictly speaking, because the speed of the cloud transport depends on the displacement magnitude of the quadrupole zero, we first change the quadrupole zero to be further away than the location of the chip's through-hole, and then make a slight adjustment during the ballistic travel to position the quadrupole zero at the chip's through-hole desired location. This final slight adjustment is in the order of $< 10\%$.

Now once the atom cloud is located inside the chip's through-hole, we turn on our mini-MOT beams (three retro-reflected MOT and repumper beams, with ≈ 1 mm beam diameter, each having a power of ≈ 0.77 mW, with a detuning of 59 MHz from (F=4 $\rightarrow$ F'=5) D2 line, quite far-detuned to reduce scattering rate). The mini-MOT beams are turned on 5 ms after the MOT beams are turned off. That is, about 5 ms before the atom cloud arrives at the chip's through-hole. After the cloud arrives at the mini-MOT, we collect about 2×10^6 atoms (50% collection efficiency) with a density of $\approx 1 \times 10^{10}$ atoms/cm^3 inside the chip's through-hole. We note that in our atom number and density calculations, we assumed the cloud has a three-dimensional Gaussian number density profile, where integrating in three-dimensions give the total atom number, and the quoted densities are the peak densities at the center of the Gaussian atom clouds.

The processes from the initial MOT cloud formation in the science chamber, to the transport towards the chip's through-hole, and collection at the mini-MOT at the chip's through-hole, are illustrated in Fig. 8.4 c) labeled (i) to (iv). The slightly diverging pushing beam (jet of atoms),

large ($\approx$ 2 cm diameter) MOT beams, and the small ($\approx$ 1 mm diameter) mini-MOT beams are also illustrated in Fig. 8.4 a,c). Figure 8.4 d) shows a photograph taken by a CCD camera from outside of the chamber, showing the chip and fluorescence of the science MOT cloud (pointed to by the white arrow). Finally in Fig. 8.4 e), the transport process from the initial science chamber MOT (labeled (i)) to the mini-MOT location (labeled (iv)) inside the chip's through-hole is shown by the absorption images taken by a CCD camera from outside of the chamber. The boundary of the chip is shown by the dashed white curves. The light beam labeled X in Fig. 8.4 c) is at normal incident to the plane of the chip (thus also the top and bottom surfaces of the nanophotonic devices). As will be discussed in Sec. 8.3, we consider atom trapping schemes where some involve external illumination light, at normal incident to the nanophotonic device. The beam labeled X in Fig. 8.4 c) illustrates a possible configuration for such trapping schemes.

8.3 Atom trapping schemes

8.3.1 Atom trapping with a single nanobeam

In this section we investigate atom trapping schemes near a single silicon nitride nanobeam. In the context of our system and given the length scales involved in our photonic structures and optical mode evanescent fields, these traps must be able to localize single atoms with sufficient reliability (sufficiently deep trap potential, relative to the atom's kinetic energy), at a location close to the surface of the dielectric nanobeam device (to allow potentially strong atom-photon coupling with the photonic mode), and preferably with minimal intrusion into the atom's internal electronic states (such as inhomogeneous broadening or transition frequency shifts). Adding to these nontrivial requirements, the trapping potential needs to be created in the presence of Casimir-Polder surface attractive potential (which induces both ground and excited state level shifts), and the trapping schemes need to conform to practical limitations (for example, trap loading schemes, atom heating and cooling, mechanical stability, optical power limit thresholds that the device can handle inside vacuum, fabrication constraints, and system geometry). Below, we give an overview of some schemes that we have considered, and show some example results that come out of our optimizations. The emphasis here is on the qualitative ideas of the schemes, and which we illustrate by our rough optimizations of the parameters. Each of the schemes has advantages and limitations across different aspects, which are of different importance depending on the overall constraints or goals (as discussed above). The results presented here are calculated using finite element analysis software COMSOL,

which computes the relevant electric field distributions of the system, and which are used in our model and approached as discussed in Sec. 7.2 (where we computed the eigenenergies of the light shift Hamiltonian, for the ground and excited states of an atom as a function of space). The coordinates used in this section correspond to the coordinate and labels discussed in Sec. 3.3 and shown in Fig. 3.11. We note that here we focus on creating trapping potential in the $x-y$ plane, orthogonal to the axis of the silicon nitride nanobeam. Depending on the exact experiments, a full three dimensional confinement, including continuous/constant or controllable axial confinement, is desired. This may be achieved for example, by having a red-detuned standing-wave trapping beam in the guided mode or with spatial patterning of the nanobeam device along the axis of the nanobeam.

8.3.1.1 Magic-compensated scheme with wavelength contrast

We start with perhaps one of the simplest schemes, similar to our nanofiber trap scheme discussed in Sec. 7.2. Consider a single nanobeam with width $w = 400$ nm and height $h = 200$ nm as shown in Fig. 3.11. We excite the y-polarized fundamental mode with a pair of counter-propagating red-detuned beams at $\lambda_{\text{red}} = 937.1$ nm with total power $P_{\text{red}} = 2\times$ 0.4 mW, and a pair of counter-propagating blue-detuned beams at $\lambda_{\text{blue}} = 686.1$ nm and 686.7 nm, where the relative detuning avoids super-lattice formation. Figures 8.5 a-b) show the resulting trap potentials[4] for along the y-axis (x=0), as a function of the atom-to-surface distance, dy. The set of curves colored in blue, red, magenta, green correspond to blue-detuned beam powers of 1, 2, 3, 10 mW each such that the total power for the counter-propagating blue-detuned beams is $P_{\text{blue}} = 2$, 4, 6, 20 mW. The thin colored curves correspond to the excited state ($6P_{3/2}$, F'=4) for Cesium, the thick colored curves correspond to the ground state ($6S_{1/2}$, F=4), which appears overlaping with the black-dashed curves that correspond to the ground state ($6S_{1/2}$, F=3). The orange curve labeled (iv) corresponds to the normalized atom-photon coupling parameter g that goes from 1 to 0, for the single nanobeam with a cavity length of $L_{\text{cav}} = 1$ mm, finesse of $\mathscr{F} = 1000$, FSR = 74 GHz (or 0.18 nm), $Q \approx 5\times10^6$, and total cavity decay rate $\kappa/2\pi = 234$ MHz. At the surface (dy=0, $x = 0$), the atom-photon coupling

[4]Here we used our model in [142], without the correction described in [64]. For Casimir-Polder potential, we use $U = -C_3/d^3$ with $C_3^g = 1160$ Hz μm^3 and $C_3^{\text{ex}} = 1705$ Hz μm^3, the coefficients for a cesium atom next to an SiO_2 plane as used in [142, 91, 64]. Note that to take into account the fact that the surface is SiN (instead of SiO_2), the coefficient C_3 should be scaled by $\frac{n2^2-1}{n2^2+1}/\frac{n1^2-1}{n1^2+1} \approx 1.70$, where n1 = 1.45 and n2 = 2.0 are SiO_2 and SiN refractive indices respectively. This scaling factor to C_3 is not taken into account in our model here. We also note that as discussed in Sec. 8.2.1, treating the SiN surface as an infinite plane instead of a finite sized nanobeam overestimates the C_3 coefficient by about a factor of three for a nanobeam with thickness 200 nm. Within these approximations and caveats, the purpose here is to present the qualitative trapping scheme and rough quantitative behavior. The trap potential calculations for all other trapping schemes described in this chapter (with the exception of this magic-compensated single-nanobeam scheme) are based on [142], without the correction of [64], with adjusted Casimir-Polder coefficients for cesium atom and silicon nitride plane, i.e., $U = -C_3/d^3$ with $C_3^g = 1.7\times1160 = 1972$ Hz μm^3 and $C_3^{\text{ex}} = 1.7\times1705 = 2899$ Hz μm^3.

rate is $g/2\pi = 1.15$ GHz, leading to a cooperativity parameter of $C \approx 540$. The dotted lines labeled (i), (ii), and (iii) correspond to the distances (dy = 138 nm, 260 nm, 392 nm) where the g parameter is equal to $4 \times \kappa$, $2 \times \kappa$, and κ respectively. Fig. 8.5 b) shows a close-up of the trap potential with $P_{\text{blue}} = 2\times$ 2 mW, forming a trap at dy $\approx$ 200 nm, with a depth of $U_{\text{trap}} \approx 400$ μK. Here, the atom-photon coupling rate, g, exceeds twice the total cavity decay rate, κ. In this scheme, as in the case of our nanofiber trap scheme, we utilize red- and blue-detuned FORT beams to provide long-range attractive and short-range repulsive potentials respectively. The length scale contrast is created by the fact that the red- and blue-detuned beams have a significantly different wavelengths and hence different evanescent field decay lengths. With the use of the magic-compensated scheme as in our nanofiber trap scheme discussed in Sec. 7.2, leading to minimal differential scalar and vector light shifts, this provides a quite good trap for our single nanobeam system. However, there is one nontrivial requirement implicit in this trap scheme, which is the use of relatively high propagating optical power $P_{\text{total}} \approx 5$ mW, which at the time of writing, is still challenging to realize in an actual lithographically fabricated nanobeam device. Typically, we have only been able to excite propagating optical power of $P_{\text{total}} \lesssim 100$ μW without breaking/melting the tiny nanobeam structure. As with the nanofiber fabrication as discussed in Sec. 7.3, given the limited thermal conductivity in vacuum environment, it is not trivial to increase the optical power threshold level. Further work is required to enable higher optical power-carrying ability inside vacuum.

8.3.1.2 Small detuning with orthogonal polarizations

One potential solution to overcome the high optical power requirement discussed above is to use much smaller detuning (e.g., few hundreds of GHz detuning) for the red- and blue-detuned beams to create similar attractive and repulsive potentials but at a lower optical power, at the expense of higher heating rate through scattering, as well as non-magic wavelength conditions. With these tradeoffs, there is still another challenge that needs to be addressed, namely the attractive and repulsive potentials must have significantly different spatial length scales such that a potential well can be formed. In this second scheme, we solve this problem by configuring the red- and blue-detuned beams to have orthogonal polarizations, and hence different decay lengths along a particular direction. Figure 8.5 c) shows the decay length scales L_x and L_y of the electric field amplitude $|E|$, $|E| = |E|_0 \exp(-dx/L_x)$ and $|E| = |E|_0 \exp(-dy/L_y)$, where $|E|_0$ is the electric field magnitude $|E|$ at the surface, dx is the atom-to-surface distance along the x-axis ($y = 0$), and dy is the atom-to-surface distance along the y-axis ($x = 0$). In this plot, the single nanobeam height is $h = 200$ nm,

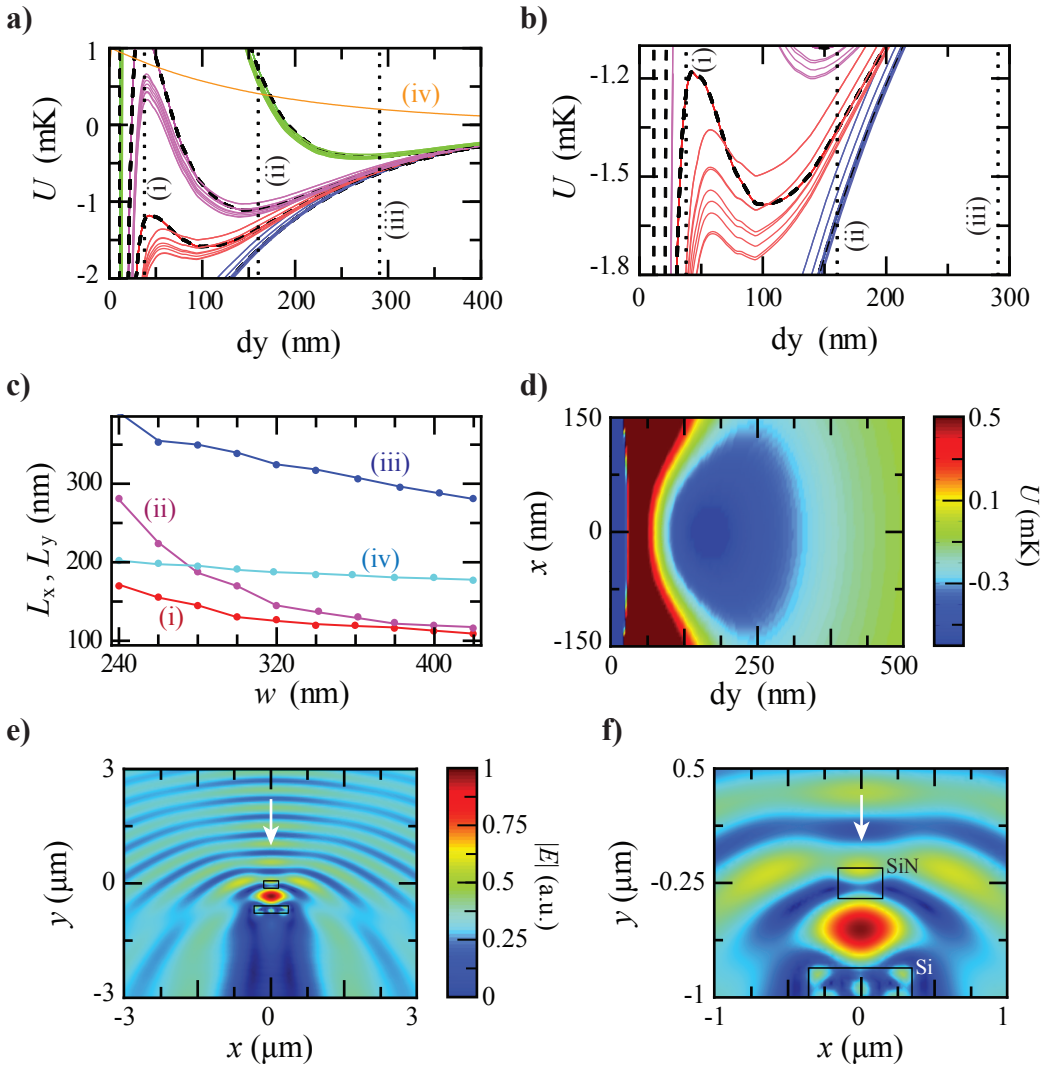

Figure 8.5: **Atom trapping schemes with a single nanobeam (part 1). a-b)** Trapping potential U for magic-compensated scheme (similar to Sec. 7.2). a) and b) show the same curves over different plot ranges. Single nanobeam width w = 400 nm, height h = 200 nm (Fig. 3.11). Red-detuned standing-wave (λ_{red} = 937.1 nm, power $P_{\text{red}} = 2\times$ 0.4 mW) and counter-propagating blue-detuned beams (λ_{blue} = 686.1 nm and 686.7 nm). dy: atom-to-surface gap along y-axis (x=0). Blue, red, magenta, green curves for $P_{\text{blue}} = 2\times \{1, 2, 3, 10\}$ mW respectively. Thin curves: excited state ($6P_{3/2}$, F'=4), thick curves: ground state ($6S_{1/2}$, F=4), black-dashed curves: ground state ($6S_{1/2}$, F=3). Orange curve (iv): normalized atom-photon coupling rate g, for a cavity length L_{cav} = 1 mm, finesse $\mathscr{F}$ = 1000, FSR = 74 GHz (or 0.18 nm), $Q \approx 5\times10^6$, and cavity decay rate $\kappa/2\pi$ = 234 MHz. At the surface (dy=0, $x = 0$), $g/2\pi$ = 1.15 GHz. Dotted lines (i), (ii), and (iii) correspond to distances (dy = 138 nm, 260 nm, 392 nm) where $g = 4\times\kappa$, $2\times\kappa$, and κ respectively. **c-d)** Trapping scheme using orthogonal polarizations. **c)** Decay lengths L_x and L_y of the electric field amplitude $|E|$, $|E| = |E|_0\exp(-dx/L_x)$ (similarly for L_y), where $|E|_0 = |E|$ at the surface. dx: atom-to-surface gap along x-axis ($y = 0$), dy: along y-axis ($x = 0$). x-polarized mode (red, magenta): (i) and (ii) for L_x and L_y respectively; y-polarized mode (blue, cyan): (iii) and (iv) for L_x and L_y respectively. Here, nanobeam height h = 200 nm, width w. **d)** Trap potential U for a red-detuned y-polarized standing wave ($\Delta\nu_{\text{red}}$ = -350 GHz, power $P_{\text{red}} = 2\times 6$ μW) and a blue-detuned x-polarized traveling wave ($\Delta\nu_{\text{blue}}$ = +350 GHz, power P_{blue} = 200 μW) for a nanobeam width w = 360 nm, height h = 200 nm, trapping along the y-axis. **e-f)** External illumination trap scheme. Plots show electric field amplitude $|E|$ of a 300 nm × 200 nm silicon nitride beam above a 700 nm × 200 nm silicon beam with vertical surface-to-surface gap of 450 nm, where a single red-detuned (λ_{red} = 937 nm) plane-wave illumination light beam polarized in the z-axis (out of page) is propagating downwards.

for various widths, w. The red and magenta curves labeled (i) and (ii) correspond to the decay lengths L_x and L_y for the x-polarized modes respectively. The blue and cyan curves labeled (iii) and (iv) correspond to the decay lengths L_x and L_y for the y-polarized modes respectively. As evident, by using orthogonally polarized red- and blue-detuned beams with small detuning (roughly same wavelength, $\lambda_{\text{red}} \approx \lambda_{\text{blue}} \approx 852$ nm), we could have a contrast in the scale lengths along the x-direction or y-direction. An example of this is shown in Fig. 8.5 d), where we use a red-detuned y-polarized standing-wave (with detuning from Cesium D2 line at $\lambda = 852$ nm of $\Delta\nu_{\text{red}}$ = -350 GHz, with total power $P_{\text{red}} = 2 \times 6$ μW) and a single blue-detuned x-polarized traveling wave (with detuning $\Delta\nu_{\text{blue}} = +350$ GHz with power $P_{\text{blue}} = 200$ μW) for a nanobeam width $w = 360$ nm, height $h = 200$ nm, trapping along the y-axis. The plot shows the ground state potential with a trap potential minimum at dy = 170 nm from the surface, with a trap depth of $U_{\text{trap}} = 620$ μK, and a trap frequency along the y direction of $f_{y,\text{trap}} = 360$ kHz and along the x direction of $f_{x,\text{trap}}$ = 325 kHz. We note that we use a simple Casimir-Polder potential of an infinite XZ planar silicon nitride surface at dy = 0, $U_{\text{CP}} = C_3'/\text{dy}^3$ (see Sec. 8.2.1). As discussed in Sec. 8.2.1, the finite planar surface associated with the beam geometry could reduce the C_3' coefficient by a factor of three. Thus, we anticipate that the blue-detuned beam power in the scheme we discuss here (where we used $U_{\text{CP}} = A \times C_3'/\text{dy}^3$ with $A = 1$) may possibly be reduced from $P_{\text{blue}} = 200$ μW (for $A < 1$, e.g., $A \approx 1/3$). We also note that as we are not using the magic wavelengths, nor have compensation configuration, this trap scheme has differential scalar shifts between the excited and ground states as well as vector shifts. We estimate a vector shift inhomogeneous broadening spread of up to 100 μK within a 50 nm radius circle around the trap minimum. This is quite large and would dramatically reduce the lifetime due to heating from scattering. We also note that the small detuning between the trapping and probing beam would require narrow spectral filters to separate the two, by orders of magnitudes in intensity contrast, which could be achieved for example by using a volume Bragg grating as we used in our nanofiber trap experiment, or even by using a filter cavity with an even narrower linewidth.

8.3.1.3 External illumination with an auxiliary nanobeam

In the next scheme shown in Fig. 8.5 e-f), we consider forming a trap potential using an external illumination red-detuned beam ($\lambda_{\text{red}} = 937$ nm) as shown by the arrow in the figure. Here, we consider a silicon nitride single nanobeam waveguide of width $w = 300$ nm and height $h = 200$ nm, and an auxiliary reflecting silicon nanobeam of size 700 nm $\times$ 200 nm, with surface-to-surface

gap of 450 nm between the bottom surface of SiN beam and top surface of Si beam. Note that the contour plots show an $x-y$ cross-section, where the waveguide axis z is going out of the page. In this scheme, the electric field magnitude $|E|$ forms a global maximum at a distance of $\approx$ 200 nm below the surface of the SiN waveguide, with an intensity ($|E|^2$) contrast of about a factor of four surrounding the maximum region as shown in Fig. 8.5 f). This local and global maximum of the red-detuned beam forms a closed attractive potential, which provides a trapping potential. There are a couple of advantages of this scheme. Firstly, one could use a magic wavelength λ_{red} = 937 nm, which suppresses differential scalar shifts. Secondly, the light simulated here is linearly polarized along the z-axis (out of the page), such that there is negligible vector shift at the trap location. Thirdly, as can be seen from the contour plots, the electric field intensity inside the SiN or Si nanobeams is significantly smaller than the trap intensity, by about a factor of four to eight. Now, to get a trap depth of 1 mK, with $\lambda_{\mathrm{red}} = 937$ nm, we need an intensity of $I_{\mathrm{red}} = 2$ mW/μm^2 (see Eq. (3.25)). We calculate that for a single nanobeam of width $w = 300$ nm, height $h = 200$ nm, with a propagating $\lambda = 852$ nm beam with optical power of 10 μW, then the peak intensity located at the center of the nanobeam in the $x-y$ cross-section is $I_{\mathrm{max}} = 174$ μW/μm^2, and the intensity at the surface is along the x-axis (y=0) is $I_{\mathrm{surf}} = 45$ μW/μm^2. As the electric field intensities at the SiN and Si nanobeams are about four to eight times smaller than the intensity at the trap location, an intensity of $I_{\mathrm{red}} = 2$ mW/μm^2 at the trap location corresponds to an intensity of I_{beam} = 250-500 μW/μm^2. If we set this intensity to be the intensity of the guided mode at the surface, $I_{\mathrm{surf}} = I_{\mathrm{beam}}$ = 250-500 μW/μm^2, then it corresponds to a guided mode total optical power of 56 - 112 μW, which is reasonably likely to be within the power threshold of the currently fabricated nanobeam devices. A more challenging problem however, is the generation of the red-detuned trapping beam, with an intensity of $I_{\mathrm{red}} = 2$ mW/μm^2. Even for a very small beam of waist radius size of 10 μm, this corresponds to a total power of around 630 mW. With this small beam size, beam pointing stability may also be an issue. We note that we have considered this case with the magic wavelength $\lambda_{\mathrm{red}} = 937$ nm. All of these requirements will relax significantly if we use smaller detuning, closer to the atomic transition 852 nm. In this case, optical power requirements will go down proportionally with detuning (see Eq. (3.25)), assuming of course that the heating rate from scattering can be kept sufficiently low, which we can for modest traps. From the fabrication side, a challenge will be to fabricate this two-vertically-stacked-nanobeams configuration. Preliminary discussions with Richard Norte, Sean Meneehan, and Justin Cohen in the Painter group concluded this is a practically plausible configuration from a fabrication perspective.

8.3.1.4 External illumination without phase coherence

In the previous scheme discussed above, we considered a single SiN nanobeam paired with an auxiliary Si nanobeam below it to form a local intensity maximum at about 200 nm from the surface of the SiN nanobeam. In this scheme, we consider a way to form a local intensity maximum for trapping atoms without the use of the auxiliary silicon nanobeam. This is achieved by having a counter-propagating red-detuned beams from the top and bottom of the SiN nanobeam, at normal incident. This is illustrated in Fig. 8.6, where we consider a single SiN nanobeam with width $w = 300$ nm and height $h = 200$ nm. We illuminate the nanobeam at normal incident along the y direction from the top and bottom, with sufficient detuning between the two such that they are phase incoherent and phase insensitive (favorable for stability). In the calculations shown in Fig. 8.6, the wavelength for the top and bottom illumination light is $\lambda_{\text{red}} = 852.55$ nm (with small $\approx$ GHz relative detuning), and the total intensity (of the plane-wave incident illumination light beams) is $I_{\text{red}} = 2 \times 32\ \mu\text{W}/\mu\text{m}^2$ (i.e., it roughly corresponds to illumination with counter-propagating Gaussian beams with a total power of $P_{\text{red}} = 2 \times 10$ mW for a beam waist radius 10 μm). The illumination light is polarized along the z-axis (out-of-page), the axis of the SiN nanobeam waveguide. Fig. 8.6 c-d) shows the $x - y$ cross-section showing the SiN nanobeam and the time-averaged total electric field magnitude $|E|$, created by the two counter-propagating phase-incoherent beams as shown by the white arrows. The line cuts along the x- (labeled (i)) and y- (labeled (ii)) axes are shown in Fig. 8.6 e-f) for over different ranges. We see from the contour and line plots that along the y-axis (i.e., at x=0), there are two closed local maxima on both sides of the nanobeam, which could be utilized to form a trap.

Figure 8.6 a) shows the calculated trap potential contour plot for the ground state of cesium, Fig. 8.6 b) shows the cross-section as a function of the atom-to-surface distance along the y-axis (x=0), dy. The red curves correspond to the excited state ($6\text{P}_{3/2}$, F'=4) for cesium, the blue curve corresponds to the ground state ($6\text{S}_{1/2}$, F=4), and the black-dashed curve corresponds to the ground state ($6\text{S}_{1/2}$, F=3). The Casimir-Polder (atom-surface) potential is included as a simple $U_{\text{CP}} = C_3'/\text{dy}^3$ (see Sec. 8.2.1), which overestimates the strength of the potential by possibly up to a factor of three. Nonetheless, with this potential, one could form a trap with depth > 2 mK at a location ≈ 125 nm from the surface of the SiN nanobeam, which is very close. This scheme is very promising, although unlike the previous scheme (Fig. 8.6 e-f)) where we have one local and global intensity maximum, here we have many significantly strong local maxima and, in particular, we have the four strongest local maxima that are close to the SiN beam. This means atoms inside the cloud could get trapped in any of these local maxima, reducing the probability of having single atoms

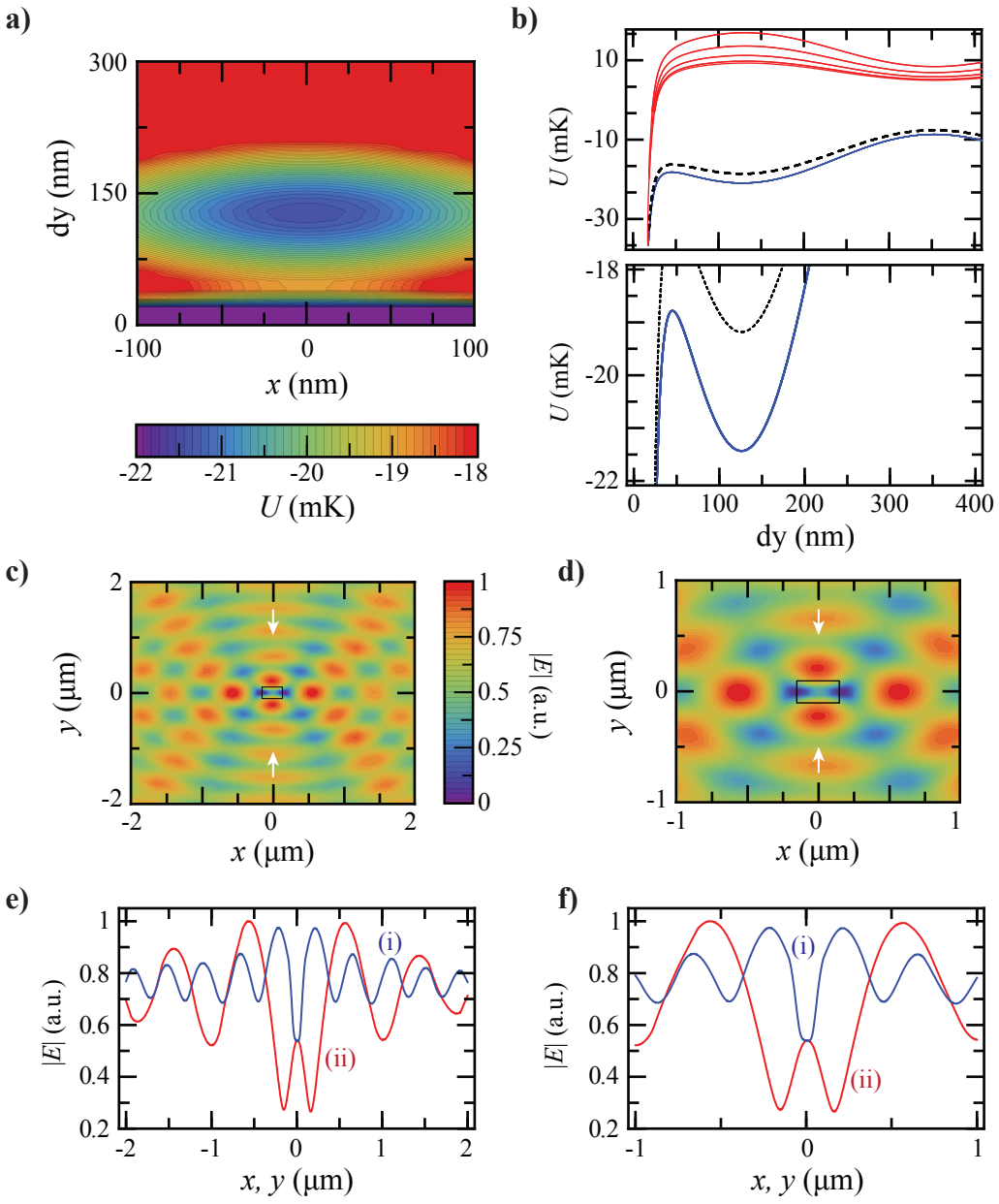

Figure 8.6: **Atom trapping schemes with a single nanobeam (part 2).** Normal incident incoherent counter-propagating red-detuned external illumination light trapping scheme. The single silicon nitride nanobeam has a width of $w = 300$ nm and height $h = 200$ nm. The external counter-propagating illumination beams have a wavelength $\lambda_{\text{red}} = 852.55$ nm with a small $\approx$ GHz relative detuning, and total intensity $I_{\text{red}} = 2 \times 32\ \mu\text{W}/\mu\text{m}^2$ (i.e., total power of $P_{\text{red}} = 2 \times 10$ mW for a beam waist radius $\approx 10\ \mu$m). **a)** Contour plot of trap potential U as a function of the x-coordinate and atom-to-surface distance along the y-axis ($x = 0$), dy. **b)** Line cut along the y-axis ($x = 0$) showing the trapping potential. The red curves correspond to cesium excited state ($6\text{P}_{3/2}$, F'=4), the blue curves correspond to the ground state ($6\text{S}_{1/2}$, F=4), and the black-dashed curves that correspond to the ground state ($6\text{S}_{1/2}$, F=3). **c-d)** Contour plots of electric field amplitude $|E|$ on the $x - y$ cross-sectional plane, where the nanobeam's waveguide axis is along the z-axis (out of page). The white arrows indicate the external illumination beams. **e-f)** Line cuts of $|E|$ of the corresponding countour plots, along the y-axis ($x = 0$) shown by the blue curves (i), and along the x-axis ($y = 0$) shown by the red curves (ii).

trapped at the trap location that we want, 125 nm close above or below the SiN nanobeam. One possible solution is to use the optical guided mode to spatially select the atoms that are near the desired trap locations to be sensitive to the trapping beams. We note that the frequency difference between the ($6S_{1/2}$, F=3) and ($6S_{1/2}$, F=4) ground states of cesium is about 9 GHz. If we use a very small red-detuning for the trapping beam, for example, 1 GHz, relative to the F=4 $\rightarrow$ F'=5 closed/cyclic state, then the atoms in F=4 ground state will feel about a 10 times stronger attractive force due to the red-detuned beam (for a given intensity), than the atoms in the F=3 ground state. By turning off the repumper beam in the mini-MOT cloud, atoms in the cloud eventually fall into the F=3 ground state. We can then inject the repumping beam (F=3 $\rightarrow$ F'=4 transition) into the y-polarized fundamental guided mode of the SiN nanobeam, which has largest field distribution at the top and bottom sides of the SiN nanobeam, and therefore repump the atoms into F=4 ground state as they decay from the F'=4 excited state. These atoms will be located near the desired trapping locations, and will be trapped as desired. We note that this process is especially required if we would like to trap as many atoms as possible near the top and bottom of the SiN nanobeam, along the axis of the nanobeam. If we have a cavity, a strong atom-photon coupling with just one atom, there may be sufficient probability to load a single atom near the desired trap location, at some location along the entire SiN nanobeam. Although loading the atoms into the trap by cooling (dissipation) is more conventional and is a good possible approach, another approach to consider in this case (assuming we have a cavity and a strong atom-photon coupling with just one single atom) is to monitor the cavity optical response in real-time, using the y-polarized guided mode, and turn on the external illumination trapping beams conditioned upon the detection of an atom, which naturally also spatially filters nearby atoms to be trapped at the desired locations. We note that as this scheme is optically phase-incoherent, and the locations of the traps are defined by the geometry of the SiN nanobeam, it has favorable robustness in relation to for example, beam pointing stability or potential mechnical vibrations of the SiN nanobeam on a chip. Overall, it is a quite promising trapping scheme that could be implemented and tested experimentally.

8.3.1.5 External illumination with phase coherence

Next, we consider a scheme similar to the above, with counter-propagating top and bottom illumination red-detuned beams as shown in Fig. 8.7 a-b), but here both beams have the exact same wavelength ($\lambda \approx 852$ nm), such that we have phase coherence. Here we will need to phase lock the two beams relative to each other and also relative to the location of the SiN nanobeam. For example,

in Figure b), the location of the SiN nanobeam is moved up (in $+y$-direction) by an amount 200 nm relative to the counter-propagating beam phases in figure a). We see that the local intensity maximum switches side from the top to the bottom of the SiN beam, as expected. While this scheme is not as good as the previous phase-incoherent scheme in terms of the phase-sensitivity, beam pointing stability and mechanical vibrations of the SiN nanobeam, if these issues can be solved by a sufficiently good stabilization, then there may be certain advantages in this scheme compared to the phase-incoherent case, for example in the atom loading process. Here, by chirping the frequency of the counter-propagating beams, we may be able to conveyor atoms that are initially loaded into a local intensity maximum trap formed by the standing-wave red-detuned beams, to the desired location close to the SiN nanobeam.

8.3.1.6 Hybrid external illumination and guided mode excitation

Here, we consider a hybrid scheme involving one external illumination red-detuned beam from the side (along x-axis, in $+x$ direction), combined with an x-polarized counter-propagating blue-detuned guided mode beam. Figures 8.7 c-f) show the calculated trapping potential as a function of the y coordinate, and the atom-to-surface distance along the x direction, dx. Here, the SiN nanobeam has a width $w = 300$ nm and height $h = 200$ nm. The red-detuned external side illumination beam has a wavelength of $\lambda_{\mathrm{red}} = 852.55$ nm (0.2 nm red-detuned from cesium transition wavelength $\lambda_{\mathrm{Cs}} = 852.35$ nm), with a power of $P_{\mathrm{red}} = 1$ mW for a beam cross-sectional radius of 10 μm, shining in the $+x$ direction, with an electric field polarized in the z-axis, parallel to the axis of the SiN nanobeam, going out-of-page in Fig. 8.7 c). The blue-detuned x-polarized guided mode beam has a wavelength of $\lambda_{\mathrm{blue}} = 852.15$ nm (0.2 nm blue-detuned from $\lambda_{\mathrm{Cs}} = 852.35$ nm), which is counter-propagating with a total power of $P_{\mathrm{blue}} = 2 \times 0.5$ μW. The counter-propagating blue-detuned beams need to be slightly detuned relative to each other, to average out standing-wave patterns to avoid anti-trapping potentials along the axial (z) direction. Some advantages of this scheme compared to the phase-incoherent illumination scheme (Fig. 8.6) are the use of a single external illumination beam instead of two, and the fact that there is only one closed trap potential formed near the surface of the SiN nanobeam, as the trap is formed by combining the transmission of the red-detuned external illumination beam through the SiN nanobeam (that has a long exponential decay length) and the blue-detuned guided mode (that has a short exponential decay length) that provides a repulsive potential. Fig. 8.7 c) shows the contour plot of the trap potential, with the cross-sections along the x-axis ($y = 0$), as a function of the atom-to-surface distance, dx, shown in Fig. 8.7 e-f). In

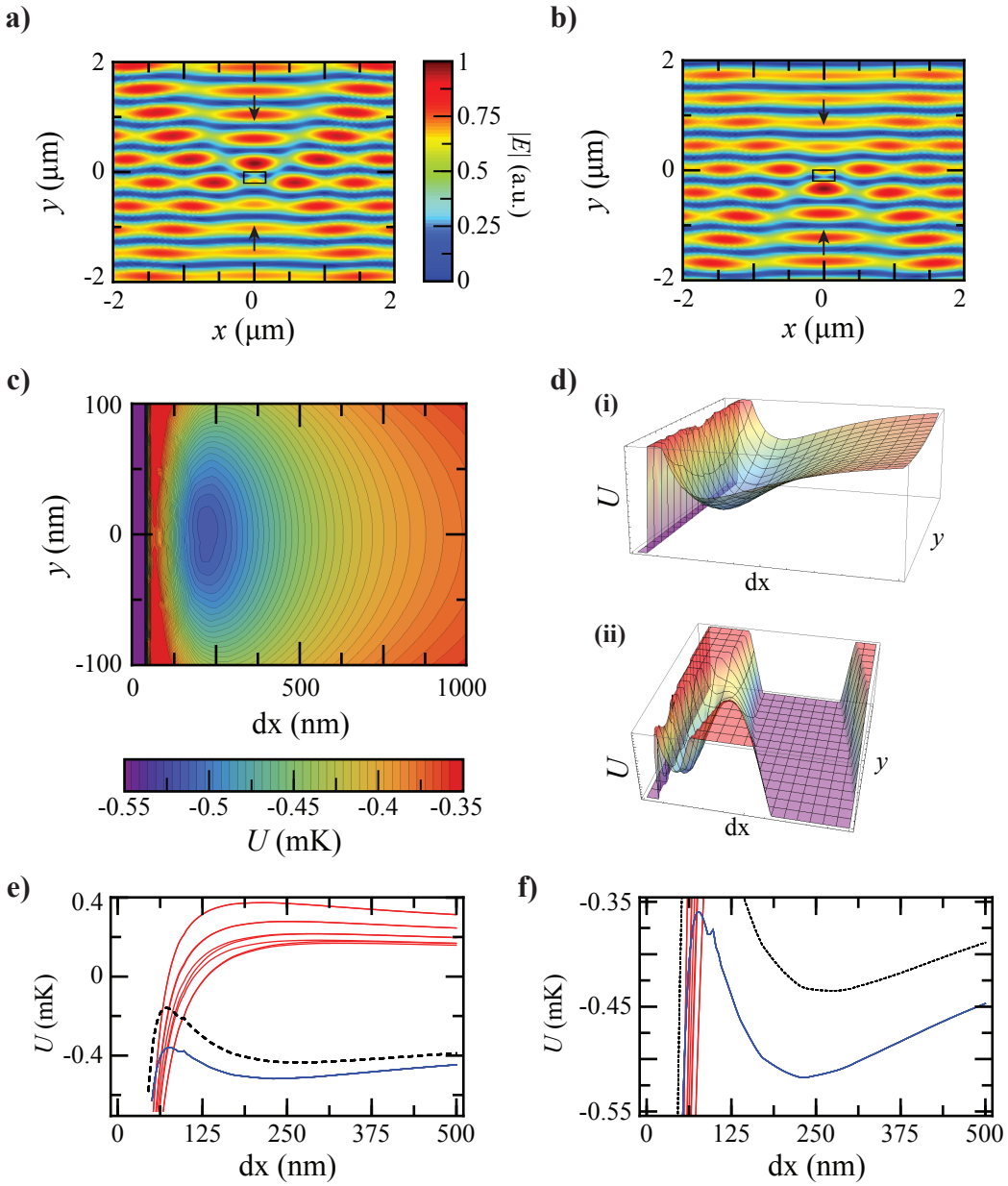

Figure 8.7: **Atom trapping schemes with a single nanobeam (part 3). a-b)** Counter-propagating coherent red-detuned beams (black arrows) forms a standing wave pattern. Single nanobeam has a width of $w = 300$ nm, height $h = 200$ nm, and the illumination light has a wavelength $\lambda \approx 852$ nm. Here the two light beams are phase-locked relative to each other, and relative to the SiN nanobeam. The phase-locked standing wave is shifted vertically along y-axis by 200 nm for plot b) relative to plot a). **c-f)** Hybrid external side illumination and guided mode trapping scheme, with same SiN nanobeam dimensions. A red-detuned side illumination beam has a wavelength of $\lambda_{\text{red}} = 852.55$ nm, a power of $P_{\text{red}} = 1$ mW for a beam cross-sectional radius of 10 μm, shining towards the $+x$ direction, with electric field polarized in the z-axis (out-of-page); and a blue-detuned counter-propagating x-polarized guided mode beam (wavelength $\lambda_{\text{blue}} = 852.15$ nm, power $P_{\text{blue}} = 2 \times 0.5$ μW). **c)** Trap potential U as a function of y coordinate and atom-to-surface distance along x-axis, dx. **d)** 3D plots illustrating the trapping potential U as a function of dx and y in (i), and in (ii), for a tilted side illumination Poynting vector, at 10° angle from the x-axis, on the $x-y$ plane. **e-f)** Line cuts of U from c), which is the same as in d) (i). Red curves: excited state ($6P_{3/2}$, F'=4), blue curves: ground state ($6S_{1/2}$, F=4), black-dashed curves: ground state ($6S_{1/2}$, F=3).

Fig. 8.7 d), a 3D potential illustration is shown in part (i), and in part (ii), the same illustration is shown but with the external incident illumination beam Poynting vector tilted by 10° relative to the x-axis. We see that a trap is still present with this tilting.

8.3.2 Atom trapping with a double nanobeam

In this section we investigate atom trapping schemes near a double silicon nitride nanobeam, as illustrated in Fig. 3.13. This section follows from the discussion at the beginning of Sec. 8.3.1. The coordinates used in this section correspond to the coordinate and labels discussed in Sec. 3.3 and shown in Fig. 3.13.

8.3.2.1 External illumination with an auxiliary nanobeam

Figures 8.8 a-b) show the electric field amplitude $|E|$ profile on the $x-y$ cross-sectional plane formed by two red-detuned beams ($\lambda_{\text{red}} = 937$ nm) shining from the $-x$ and $+x$ directions, tilted by $\theta = 15°$ from the horizontal axis as shown by the white arrows. The two beams are phase-coherent, their electric field is polarized along the z-axis, parallel to the double nanobeam axis (out of the page). The double nanobeam consists of two silicon nitride rectangular waveguides each with a width $w =$ 300 nm and height $h = 200$ nm, separated by a gap of 400 nm along the x-direction. The auxiliary nanobeam at the bottom has a width of 400 nm and a height of 200 nm, also made of silicon nitride material. The vertical surface-to-surface gap between the double nanobeam and the auxiliary beam below is 600 nm. We see that in this scheme, a center local and global intensity maximum is formed at the center between the SiN double nanobeam structure. This allows trapping of single atoms at a location where it could couple quite strongly to the double nanobeam guided mode (see for example, Fig. 3.14). This scheme however requires fabrication of the triple beam structure, as well as phase-locking of the illumination beams relative to each other and relative to the SiN nanobeams location.

8.3.2.2 Corrugated double nanobeam

In this scheme, we consider an infinite periodic structure with a single cell of the periodic structure shown in Fig. 8.8 c-h). The coordinate system is shown in Fig. 8.8 d). The corrugated double silicon nitride nanobeams have the following dimensions: total periodic cell (structure) length, d1 = 1 μm, total thickness, d2 = 200 nm, the width of the larger beam, d3 = 200 nm, the width of the center beam, d4 = 100 nm, the length of the center beam, d6 = 500 nm (centered along the periodic

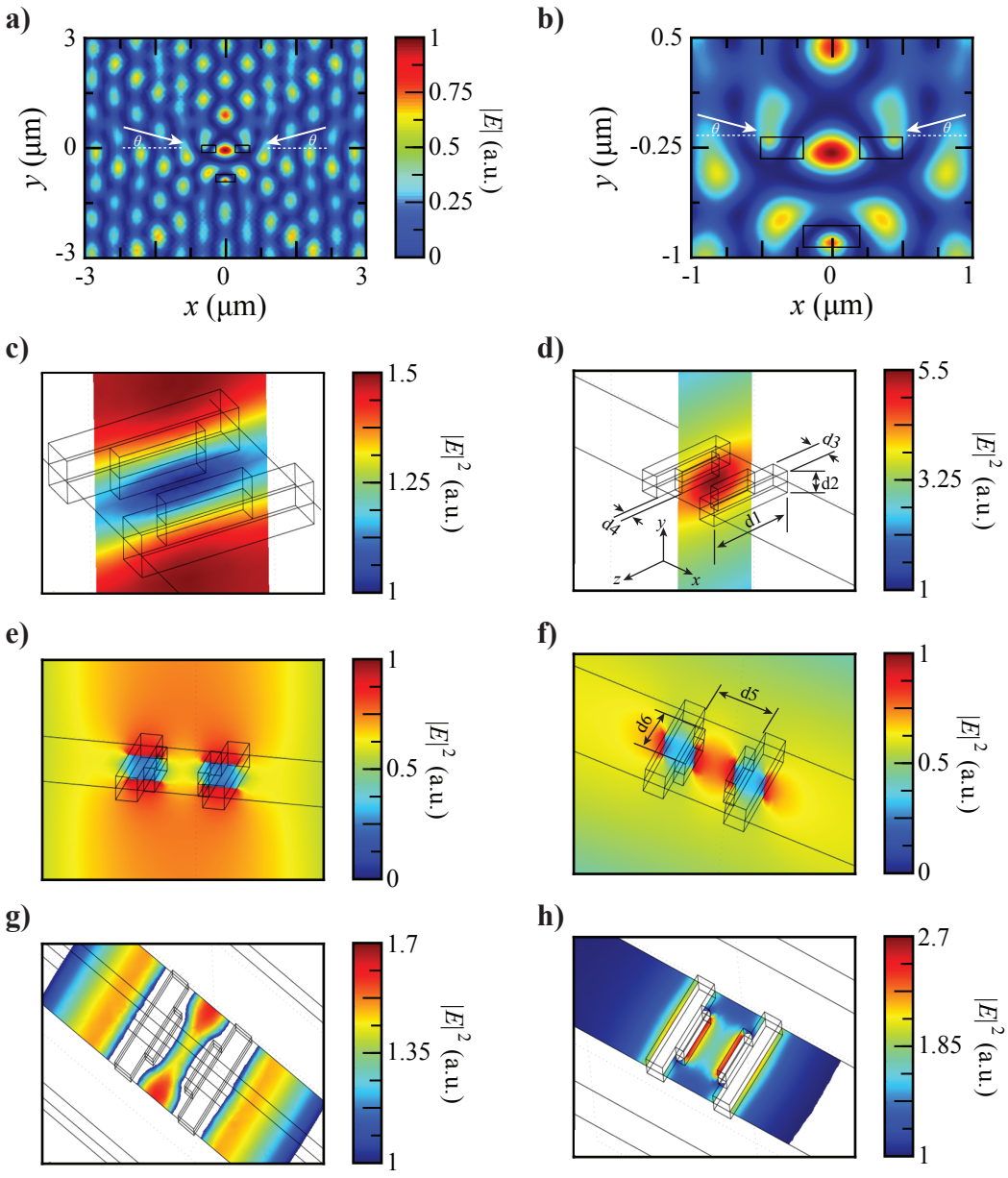

Figure 8.8: **Atom trapping schemes with a double nanobeam (part 1). a-b)** Coherent side illumination with an auxiliary beam. Here we consider two red-detuned beams ($\lambda_{\text{red}} = 937$ nm, polarized along the z-axis, out of page) shining from the $-x$ and $+x$ directions, tilted by $\theta = 15°$ from the horizontal axis as shown by the white arrows. Double beam parameters: (each beam: width $w = 300$ nm, height $h = 200$ nm) separated by a gap of 400 nm along the x-direction. The auxiliary SiN nanobeam (width 400 nm, height 200 nm) is 600 nm below the double nanobeam (surface-to-surface). **c-h)** Corrugated double SiN nanobeam trapping scheme. Cross-sectional contour plots for a propagating wavelength around 852 nm, calculated in 3D with periodic boundary condition. Total periodic cell length, d1 = 1 μm, thickness, d2 = 200 nm, width of the larger beam, d3 = 200 nm, width of the center beam, d4 = 100 nm, length of the center beam, d6 = 500 nm (centered along the periodic structure axis, i.e., along d1, z-axis), and the surface-to-surface inner gap between the larger beams, d5 = 600 nm. The coordinate system $\{x, y, z\}$ is shown in d). **c,e,g)** show a y-polarized mode, where we see a local intensity minimum in three-dimensions as shown in the $y-z$, $x-y$, $x-z$ cross-sectional planes in c), e), g) respectively. **d,f,h)** show an x-polarized mode, where here we see a local intensity maximum in three-dimensions as shown in the $y-z$, $x-y$, $x-z$ cross-sectional planes in d), f), h) respectively.

structure axis, i.e., along d1, z-axis), and the surface-to-surface inner gap between the larger beams, d5 = 600 nm. This calculation was done for a propagating wavelength around 852 nm, using full 3D calculation in COMSOL, with a Floquet periodic boundary condition. Figures 8.8 c,e,g) show a y-polarized mode, where we see a local intensity minimum in three-dimensions as shown in the $y-z$, $x-y$, $x-z$ cross-sectional planes in c), e), g) respectively. Figures 8.8 d,f,h) show an x-polarized mode, where here we see a local intensity maximum in three-dimensions as shown in the $y-z$, $x-y$, $x-z$ cross-sectional planes in d), f), h) respectively. Early discussions with Sean Meneehan, Justin Cohen, and Richard Norte from Painter group concluded that this is a plausible structure from the fabrication perspective. At this early time we would like to avoid adding more design complications beyond a simple single nanobeam or double nanobeam structure, so we did not further pursue this investigation, but we have tried to find other potential trapping schemes involving simple single or double nanobeam structures, as discussed in the subsequent sections below.

8.3.2.3 Guided mode with a blue trap

In this scheme we use a simple double nanobeam structure as shown in Fig. 3.13, where each nanobeam has a width $w = 300$ nm, height $h = 200$ nm, and the gap between the two along the x direction is 200 nm. Figure 8.9 shows trap potential profiles for this scheme, using a counter-propagating red-detuned beam with wavelength $\lambda_{\text{red}} = 853$ nm and total power $P_{\text{red}} = 2\times\ 10\ \mu$W, in the x-polarized even mode (the mode labeled (i) in Fig. 3.13 b,d)). The counter-propagating red-detuned beam forms a standing wave, which provides trapping along the axial beam direction (z-axis, out-of-page direction). For trapping in the transverse direction ($x-y$ cross-sectional plane), we utilize a single (travelling-wave) blue-detuned beam with wavelength $\lambda_{\text{blue}} = 851$ nm and total power $P_{\text{blue}} = 4$ mW in the y-polarized odd mode (the mode labeled (iv) in Fig. 3.13 b,d)). Contour plots of the trap potential U in the $x-y$ and $x-z$ planes for this configuration and parameters are shown in Fig. 8.9 a) and b). Figures 8.9 d) and f) show the line cuts of the potentials along the z-axis ($x = y = 0$) and x-axis ($y = z = 0$) respectively. The horizontal line in Fig. 8.9 f) corresponds to $U = 0$, which is the trap potential at the nodes of the red-detuned standing-wave as shown in ig. 8.9 d). The red curves correspond to the excited state ($6P_{3/2}$, F'=4) for cesium, the blue curves correspond to the ground state ($6S_{1/2}$, F=4), and the black-dashed curves correspond to the ground state ($6S_{1/2}$, F=3) in Figures 8.9 d-g). Fig. 8.9 c) shows the ground state ($6S_{1/2}$, F=4) potential U along the x-axis ($y = z = 0$) and y-axis ($x = z = 0$) with curves colored in red and blue respectively. The trap in this configuration is particularly tight. For the ground state ($6S_{1/2}$, F=4), the trap

frequencies along $\{x, y, z\}$, are $\{f_x, f_y, f_z\} = \{1.9, 3.7, 1.3\}$ MHz. This is obtained by fitting the line cut potential profiles to $U = \frac{1}{2} m_{\mathrm{Cs}} \omega^2 x^2$, where m_{Cs} is the cesium atom mass, $\omega = 2\pi f$ is the angular trap frequency (where f is the quoted values $\{f_x, f_y, f_z\} = \{1.9, 3.7, 1.3\}$ MHz), and x is the spatial coordinate, replaced by y or z correspondingly. The position uncertainty of the ground state wavefunction is $\{\Delta_x, \Delta_y, \Delta_z\} = \{4.5, 3.2, 5.5\}$ nm. This is obtained by $\Delta_x = \sqrt{\hbar/(2 m_{\mathrm{Cs}} 2\pi f_x)}$ where f_x is the trap frequency along the spatial coordinate x, replaced by y or z correspondingly. The motional harmonic ladder energy spacings are $\{\delta E_x, \delta E_y, \delta E_z\} = \{90.9, 177.7, 61.0\}$ μK respectively. They are calculated by $\delta E_x = 2\pi\hbar f_x / k_{\mathrm{B}}$, where f_x is the trap frequency along the spatial coordinate x direction, replaced by y and z correspondingly, and k_{B} is the Boltzmann constant to convert the energy to temperature unit. The trap depth is shallowest along the x-direction, which sets the overall trap depth of this configuration to $U_{\mathrm{trap}} = 2.4$ mK.

Note: The trap potential calculation in this section is based on [142], without the correction of [64], with adjusted Casimir-Polder coefficients for the cesium atom and silicon nitride plane, i.e., $U = -C_3/d^3$ with $C_3^{\mathrm{g}} = 1.7 \times 1160 = 1972$ Hz μm^3 and $C_3^{\mathrm{ex}} = 1.7 \times 1705 = 2899$ Hz μm^3, applied to both silicon nitride surfaces of the double nanobeam ($y - z$ planes at $x = -100$ nm and $x = 100$ nm). See footnote in Sec. 8.3.1.1.

Now, since in the above scheme the blue-detuned mode is a traveling wave mode, we do have vector shifts associated with this blue-detuned mode which are not canceled or compensated. However, note that this blue-detuned mode which generates a blue-trap on the $x - y$ cross-sectional plane, has a local minimum (zero field) at the center ($x = y = 0$). Moreover, as this mode is a y-polarized, odd mode, (see Fig. 3.13 d) iv)), we also have zero fields along the x ($y = 0$) and y ($x = 0$) axes. Together, this leads to vector shifts that are smaller than in a red-trap or two-color trap. Fig. 8.9 e) shows the potential U for the radius $r = 25$ nm (where $r = 0$ at the origin, located at $x = y = 0$, the center of the gap between the two SiN nanobeams), as a function of the azimuthal angle ϕ in the $x - y$ plane (where $\phi = 0$ for $x > 0, y = 0$, $\phi = 45°$ along the line $y = x$ for positive x and y, and $\phi = 90°$ for $y > 0, x = 0$). We see from the plot that the inhomogeneous broadening due to the vector shifts are largest at $\phi = 45°$ as expected, since this is the angle where the blue-detuned mode field is strongest. Figure 8.9 g) shows a close-up version of Fig. 8.9 e) for ϕ between 43° and 47°. Finally in Fig. 8.9 h) we show the inhomogeneous broadening (end-to-end) spread ΔU for $\phi = 45°$ as a function of radius r in frequency units.

Now as discussed, the above scheme/configuration involves vector shifts associated with the blue-detuned travelling wave mode. We note that this vector shift can be suppressed by implementing

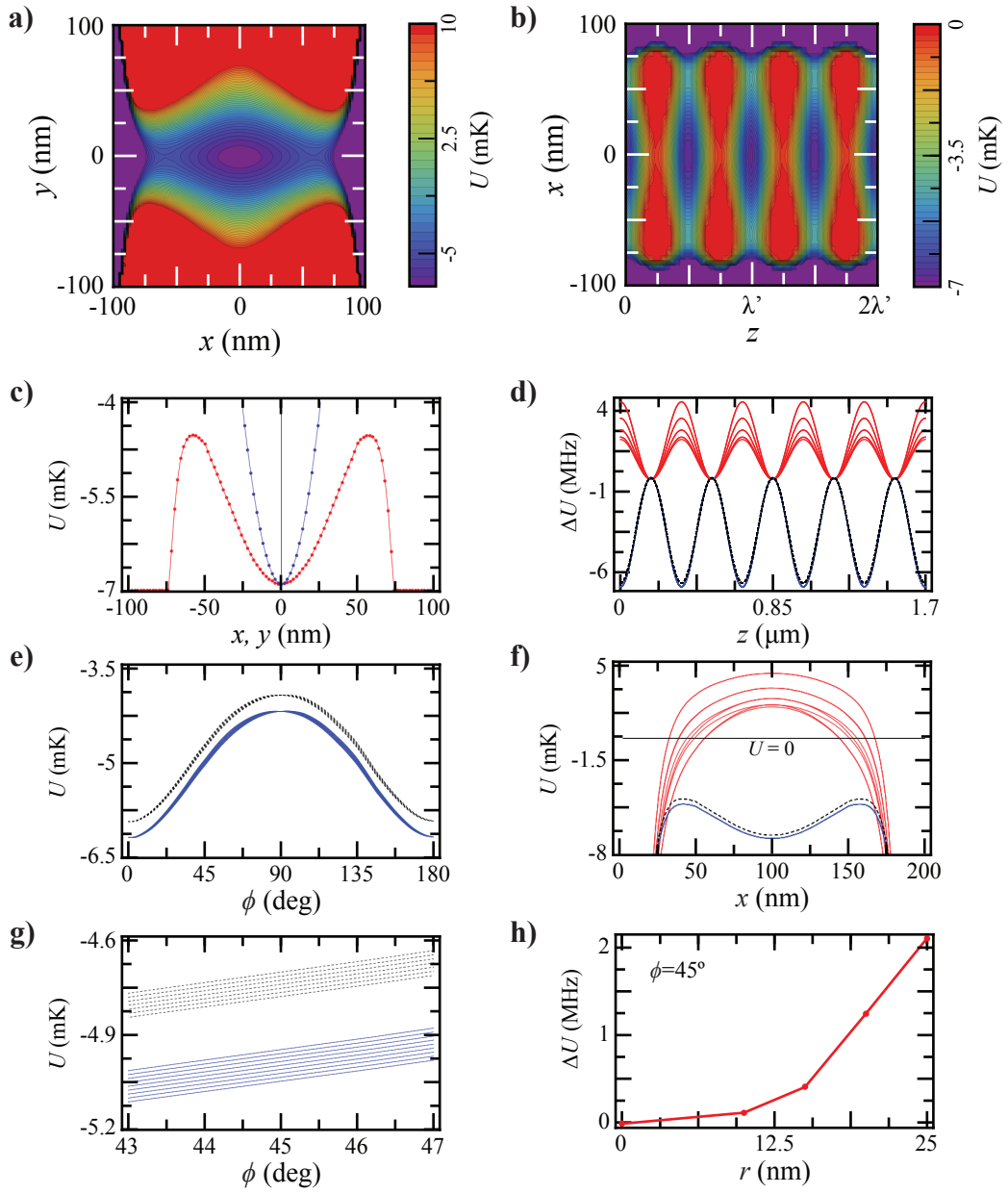

Figure 8.9: **Atom trapping schemes with a double nanobeam (part 2).** Scheme utilizes red- and blue-traps in guided modes. Double SiN nanobeam parameters: each beam: width $w = 300$ nm, height $h = 200$ nm, gap between the two along x direction is 200 nm. **a-g)** Trap potential U formed by a counter-propagating red-detuned x-polarized beams (wavelength $\lambda_{\rm red} = 853$ nm, power $P_{\rm red} = 2\times\ 10\ \mu$W) providing axial ($z$-axis, out-of-page) confinement; and a single (traveling wave) y-polarized blue-detuned beam (wavelength $\lambda_{\rm blue} = 851$ nm, power $P_{\rm blue} = 4$ mW) for transverse confinement. Casimir-Polder potential: $U = -C_3/d^3$ with $C_3^{\rm g} = 1972$ Hz μm^3 and $C_3^{\rm ex} = 2899$ Hz μm^3, for two $(y-z)$ SiN planes located at $x = -100$ nm and $x = 100$ nm. **a,b)** Potential U in the $x-y$ and $x-z$ planes. **d,f)** Line cuts along z-axis ($x = y = 0$) and x-axis ($y = z = 0$) respectively. Horizontal lines in f): $U = 0$. Red curves: excited state ($6P_{3/2}$, F'=4), blue curves: ground state ($6S_{1/2}$, F=4), black-dashed curves: ground state ($6S_{1/2}$, F=3) in d-g). Part c) shows the ground state ($6S_{1/2}$, F=4) potential U line cuts along x-axis ($y = z = 0$) and y-axis ($x = z = 0$) with curves colored in red and blue respectively. **e)** Potential U for the radius $r = 25$ nm (where $r = 0$ at the origin, located at $x = y = 0$, the center of the gap between the two SiN nanobeams), as a function of the azimuthal angle ϕ in the $x-y$ plane (where $\phi = 0$ for $x > 0, y = 0$, $\phi = 45°$ along the line $y = x$ for positive x and y, and $\phi = 90°$ for $y > 0, x = 0$). The inhomogeneous broadening due to the vector shifts are largest at $\phi = 45°$. **g)** Close-up version of part e) for ϕ between 43° and 47°. **h)** Inhomogeneous broadening spread ΔU for $\phi = 45°$ as a function of radius r.

a modification to the scheme discussed above. Here we discuss two potential modifications that could lead to suppression of these vector shifts. Firstly, we could suppress the vector shifts by making the blue-detuned mode a standing-wave, for example by implementing a photonic crystal mirror at the end of the waveguide to reflect the y-polarized blue-detuned mode. This however, will lead to leakage channels at the nodes of the blue-detuned standing wave, where no transverse confinement is present. To overcome this problem, we could implement a second blue-detuned standing wave, with a small relative detuning, such that over a certain length, the two blue-detuned standing waves are $\lambda'/2$ out-of-phase (the prime indicates the wavelength inside the waveguide mode, which is about 1.25 times smaller than the free-space wavelength for our particular configuration), eliminating the node locations, providing transverse confinement continuously along this length. For example, we consider the first blue-detuned standing wave of (free-space) wavelength $\lambda_{\text{blue1}} = 851$ nm, $\lambda'_{\text{blue1}} \approx \lambda_{\text{blue1}}/1.25 = 680.8$ nm in the waveguide, and the second blue-detuned standing wave of (free-space) wavelength $\lambda_{\text{blue2}} = 851.15$ nm, $\lambda'_{\text{blue2}} \approx \lambda_{\text{blue2}}/1.25 = 680.92$ nm in the waveguide, that is, 60 GHz relative detuning. Here, the beat-note between the two leads to a wavepacket wavelength (inside the waveguide) of $\lambda_{beat} = 3.86$ μm. Thus, the length along the waveguide axis where the two standing waves are $\lambda'/2$ out-of-phase by about 4.5°, is 48.2 μm. This is the length (per beat-note period) where the two standing-waves compliment each other and provide continuous transverse confinement along the axial z direction, allowing closed atom trapping potentials.

Another approach that could suppress the vector shifts associated with the blue-detuned trapping beam is to implement butt-coupling on both sides of the double nanobeam structure. In this case, we could then implement the compensation scheme similar to the scheme for our nanofiber trap (see Sec. 7.2), where we have two counter-propagating travelling wave blue-detuned beams which are slightly detuned relative to each other, avoiding super lattice formation, but allowing the suppression of the vector shifts associated with the blue-detuned trapping beams. With this approach, we could have a continuously uninterrupted transverse confinement of atom trapping potential. This however requires fiber to SiN waveguide butt couplings on both sides of the double nanobeam device. Although it may be practically plausible in terms of fabrication, this requires further investigation on the fabrication side.

8.3.2.4 Two-color trap with RF switching

In the previous scheme discussed in Sec. 8.3.2.3, we utilized the lowest x-polarized even mode of the double SiN nanobeam waveguide structure for the red-detuned light and the (fourth lowest) y-

polarized odd mode for the blue-detuned light (see Fig. 3.13). The excitation of these two particular supermodes of the double beam structure requires spatial and optical phase filtering, for example involving the shifting of optical phase of one of the beams to the other beam by $\lambda/2$, to excite the odd-mode. There are potential ways to realize this, which we considered, but have not mentioned here. However, in the scheme discussed in this section, the idea is to avoid this requirement, and utilize only the lowest supermode, the x-polarized even mode (the mode labeled (i) in Fig. 3.13 b,d)). As can be seen in Fig. 3.13 d) i), the electric field intensity exhibits a local minimum at the center ($x = 0$) along the x-axis (y=0), and it exhibits a local maximum at the center ($y = 0$) along the y-axis (x=0). This leads to a trapping (anti-trapping) potential for a red-detuned light along the y-axis (x-axis), and an anti-trapping (trapping) potential for a blue-detuned light along the y-axis (x-axis), saddle trap potentials. Switching between these two cases of red-detuned and blue-detuned cases at a sufficiently fast rate (which depends on the trapping frequencies) could lead to the formation of a stable pseudo-trap for a neutral atom, analogous to a quadrupole or Paul trap [183, 88, 135, 212]. This trap scheme is illustrated in Fig. 8.10 a) where the trap potential U is shown in 3D plots, the arrows between the plots illustrate the cycling directions of the sequence going from one saddle trap (trapping along y-axis and anti-trapping along x-axis) to the other (trapping along x-axis and anti-trapping along y-axis) as the trapping beam is sinusoidally alternated between red-detuned and blue-detuned beams respectively. The plot axes are shown in Fig. 8.10 a) (iii). We note that in this scheme, there is an oscillation of the potential energy as one switches from the red-detuned to blue-detuned case, which (assuming the switching frequency is far from the trap frequencies) should not cause large heating of the trapped atoms. The 3D potential plots shown in Fig. 8.10 a) are for the effective potential δU, where we subtract this oscillating potential offset such that at $x = y = 0$, the effective potential is zero, $\delta U = 0$, i.e., $\delta U = U(x, y) - U(x = y = 0)$, such that $\delta U(x = y = 0) = 0$ at all time.

In Fig. 8.10, we consider the two-color switching trap for a double Si nanobeam structure where each beam has a width w = 300 nm, height h = 200 nm, and the gap between the two beams along the x-axis is 200 nm. Fig. 8.10 a) shows an illustration of the temporal sinusoidal oscillation from the maximum blue-detuned beam intensity at time t_{blue}, (i), with a trap along the x-axis and an anti-trap along y-axis, through the transition period at time t_{both}; (ii) to (iv), to maximum red-detuned beam intensity (zero blue-detuned beam intensity) at time t_{red}, (v), followed by the reverse cycle (arrows). The time-dependent offset $U(x = y = 0)$ ranges from -0.86 mK (at time t_{red}; (v) in a) to +6.25 mK (at time t_{blue}, (i) in a). On the $x - y$ plane, the origin ($x = y = 0$)

is at the symmetry center between the two double beams. In figures 8.10 b,d), the trap potential U is formed by a counter-propagating standing wave blue-detuned beam, with wavelength $\lambda_{\text{blue}} = 851$ nm, and total power $P_{\text{blue}} = 2 \times 20$ μW. The origin ($x = y = 0$) is set to be the symmetry center between the two double beams. In Fig. 8.10 d), the red curve (labeled (i)) corresponds to the line cut potential along the x-axis ($y = 0$) and the blue curve (labeled (ii)) corresponds to the line cut potential along the y-axis ($x = 0$). Figures 8.10 c,e) show the trap potential U formed by a counter-propagating standing wave red-detuned beam, with wavelength $\lambda_{\text{blue}} = 853$ nm, and total power $P_{\text{blue}} = 2 \times 1$ μW. The origin ($x = y = 0$) is set to be the symmetry center between the two double beams. In Fig. 8.10 e), the red curve (labeled (i)) corresponds to the line cut potential along the x-axis ($y = 0$) and the blue curve (labeled (ii)) corresponds to the line cut potential along the y-axis ($x = 0$). Finally we note that the trap potential along the waveguide axis (z-axis, out-of-page direction), for example, at $z = 0$ (defined by the location of the anti-node of the standing wave), is also alternating between a trapping potential (red-detuned standing-wave) and an anti-trapping potential (blue-detuned standing-wave); and the opposite at the node location, $z = \lambda'/2$, where the prime indicates the wavelength corresponding to the waveguide mode (in this configuration, about 1.25 smaller than the free-space wavelength, $\lambda' = \lambda/1.25$).

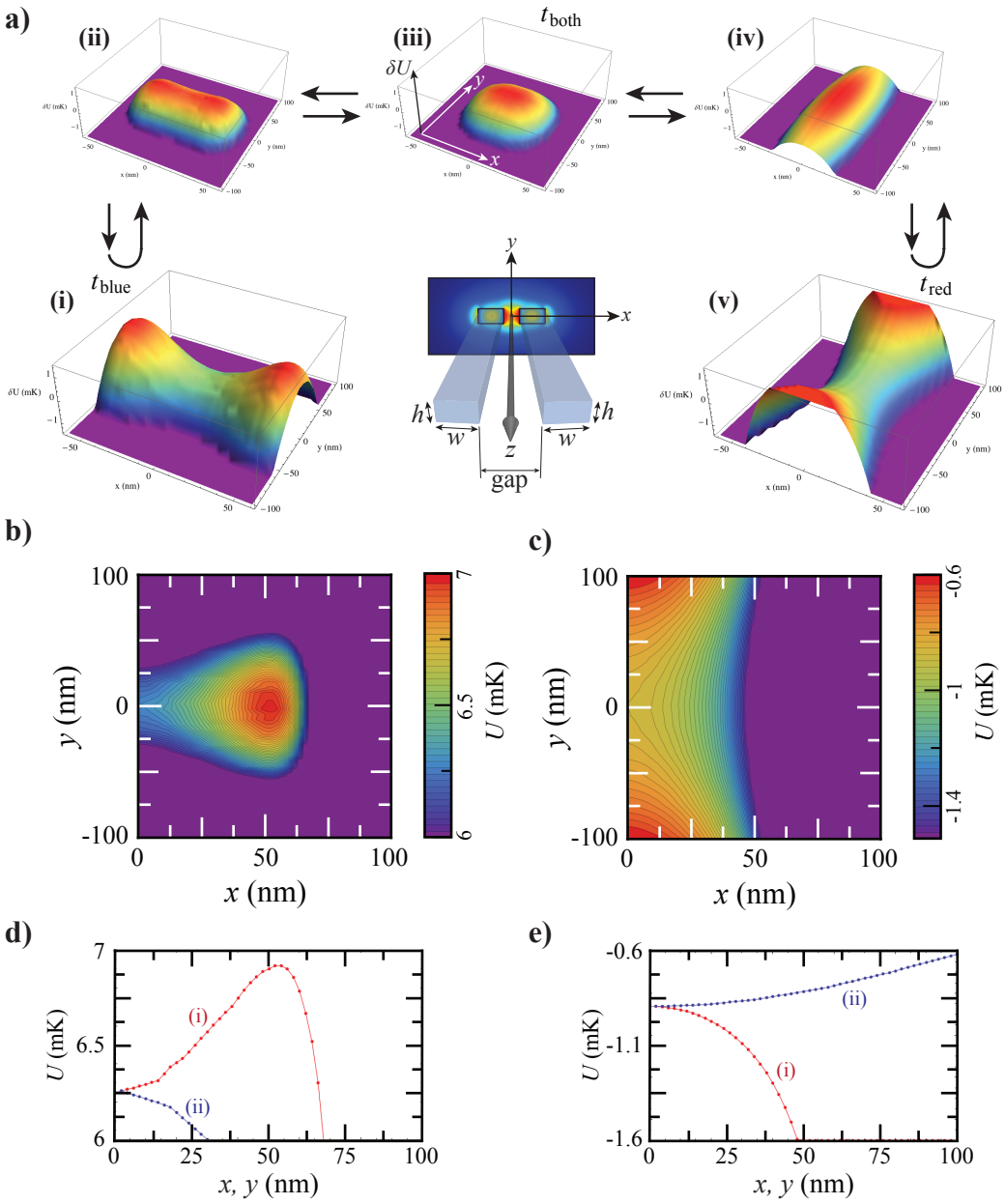

Figure 8.10: **Atom trapping schemes with a double nanobeam (part 3).** Two-color RF switching scheme. Double Si nanobeam parameters: (each: width $w = 300$ nm, height $h = 200$ nm), gap along the x-axis is 200 nm. Switching between red- and blue-detuning for an x-polarized even mode forms a pseudo trap potential analogous to a quadrupole Paul trap in ion trap systems. **a)** Illustration of sinusoidal oscillation between maximum blue-detuned beam intensity at time t_{blue}, (i), with a trap along x-axis and an anti-trap along y-axis, transition time through t_{both}, (ii) to (iv), to maximum red-detuned beam intensity (zero blue-detuned beam intensity) at time t_{red}, (v), followed by the reverse cycle (arrows). In part a), the effective potential δU corresponds to the trapping potential using the parameters described below, with offset applied to the potential U, i.e., $\delta U = U(x, y) - U(x = y = 0)$, such that $\delta U(x = y = 0) = 0$ at all time. The time-dependent offset $U(x = y = 0)$ ranges from -0.86 mK (at time t_{red}, (v) in a)) to +6.25 mK (at time t_{blue}, (i) in a)). On the $x - y$ plane, the origin ($x = y = 0$) is at the symmetry center between the two double beam. **b,d)** Trap potential U formed by a standing wave blue-detuned beam (wavelength $\lambda_{\text{blue}} = 851$ nm, power $P_{\text{blue}} = 2 \times 20$ μW). **d)** Red curve (i): line cut along x-axis ($y = 0$). Blue curve (ii): line cut along y-axis ($x = 0$). **c,e)** Trap potential U formed by a standing wave red-detuned beam (wavelength $\lambda_{\text{blue}} = 853$ nm, power $P_{\text{blue}} = 2 \times 1$ μW). **e)** Red curve (i): line cut along x-axis ($y = 0$). Blue curve (ii): line cut along y-axis ($x = 0$).